การศึกษาสนามไฟฟ้าที่จุดสัมผัสมุมศูนย์ระหว่างฉนวนสามชนิด

นาย ฮุย เวียต ควอค

วิทยานิพนธ์นี้เป็นส่วนหนึ่งของการศึกษาตามหลักสูตรปริญญาวิศวกรรมศาสตรมหาบัณฑิต
สาขาวิชาวิศวกรรมไฟฟ้า ภาควิชาวิศวกรรมไฟฟ้า
คณะวิศวกรรมศาสตร์ จุฬาลงกรณ์มหาวิทยาลัย
ปีการศึกษา 2553

STUDY OF ELECTRIC FIELD AT A ZERO-ANGLE CONTACT POINT BETWEEN THREE DIELECTRICS

Mr. Huynh Viet Quoc

A Thesis Submitted in Partial Fulfillment of the Requirements
for the Degree of Master of Engineering Program in Electrical Engineering
Department of Electrical Engineering
Faculty of Engineering
Chulalongkorn University
Academic Year 2010

Thesis Title	STUDY OF ELECTRIC FIELD AT A ZERO-ANGLE CONTACT POINT BETWEEN THREE DIELECTRICS
By	Mr. Huynh Viet Quoc
Field of Study	Electrical Engineering
Thesis Advisor	Associate Professor Boonchai Techaumnat, Ph.D.

Accepted by the Faculty of Engineering, Chulalongkorn University in Partial Fulfillment of the Requirements for the Master's Degree

.... Dean of the Faculty of Engineering

(Associate Professor Boonsom Lerdhirunwong, Dr.Ing.)

THESIS COMMITTEE

.... Chairman

(Assistant Professor Komson Petcharaks, Ph.D.)

.... Thesis Advisor

(Associate Professor Boonchai Techaumnat, Ph.D.)

.... Examiner

(Channarong Banmongkol, Ph.D.)

A.PRUKSANUBAL

.... External Examiner

(Aphibul Pruksanubal, Ph.D.)

สุย เวียด ควอค : การศึกษาสนามไฟฟ้าที่จุดสัมผัสมุมศูนย์ระหว่างฉนวนสามชนิด. (STUDY OF ELECTRIC FIELD AT A ZERO-ANGLE CONTACT POINT BETWEEN THREE DIELETRICS) อ. ที่ปรึกษาวิทยานิพนธ์หลัก : รศ. ดร. บุญชัย เตชะอำนาจ, 60 หน้า.

ระบบจ่ายไฟฟ้าเหนือดินในประเทศไทยนำเอาสายเคเบิลอากาศมาใช้อย่างแพร่หลาย เพื่อพัฒนาความน่าเชื่อถือของระบบ ปัญหาทั่วไปที่พบบ่อยในระบบสายเคเบิลอากาศคือฉนวนของสายเคเบิลอากาศเกิดความเสียหายขึ้น ณ ตำแหน่งที่สัมผัสกับสเปเซอร์ สาเหตุที่เป็นไปได้อาจเกิดจากการเกิดดีสชาร์จบางส่วนขึ้น ณ ตำแหน่งจุดสัมผัสระหว่างสายเคเบิลอากาศกับสเปเซอร์ เนื่องจากสนามไฟฟ้าที่บริเวณดังกล่าวมีค่าสูง วิทยานิพนธ์นี้ศึกษาการเพิ่มขึ้นของสนามไฟฟ้าใกล้จุดสัมผัสซึ่งเป็นจุดสัมผัสมุมศูนย์ โดยรูปแบบการเรียงที่ใช้ได้แก่ ตัวนำหุ้มฉนวนและฉนวนแข็ง แทนสายเคเบิลอากาศและสเปเซอร์ตามลำดับ วัตถุประสงค์ของวิทยานิพนธ์คือศึกษาความสัมพันธ์ระหว่างสนามไฟฟ้าที่เพิ่มขึ้นกับตัวแปรของรูปแบบการจัดเรียงที่ใช้ ได้แก่ อัตราส่วนของความหนาของฉนวนแข็งต่อรัศมีของตัวนำหุ้มฉนวน โดยเปรียบเทียบกับกรณีที่ใช้ค่าคงที่ไดอิเล็กตริกของวัสดุต่างชนิดกัน การศึกษาการเปลี่ยนแปลงของสนามไฟฟ้าที่จุดสัมผัสโดยใช้รูปแบบการจัดเรียงซึ่งมีการแทรกชั้นของตัวนำ หรือฉนวนระหว่างตัวนำหุ้มฉนวนกับฉนวนแข็ง ทำหน้าที่ลดการเพิ่มขึ้นของสนามไฟฟ้า วิธีที่ใช้ในการคำนวณสนามไฟฟ้าคือวิธีเงามัลติโพลสำหรับบริเวณสองมิติซึ่งวิธีเชิงวิเคราะห์ที่ให้คำตอบซึ่งมีความแม่นยำสูง

ภาควิชา ....วิศวกรรมไฟฟ้า..... ลายมือชื่อนิสิต..
สาขาวิชา.........วิศวกรรมไฟฟ้า..... ลายมือชื่อ อ.ที่ปรึกษาวิทยานิพนธ์หลัก ....
ปีการศึกษา ....2553....................

527 07254 21 : MAJOR ELECTRICAL ENGINEERING

KEYWORDS : ELECTRIC FIELD / ZERO-CONTACT ANGLE / TRIPLE JUNCTION / METHOD OF IMAGES / MULTIPOLE RE-EXPANSION / FLOATING CONDUCTOR

HUYNH VIET QUOC : STUDY OF ELECTRIC FIELD AT A ZERO-ANGLE CONTACT POINT BETWEEN THREE DIELECTRICS. ADVISOR : ASSOC. PROF. BOONCHAI TECHAUMNAT, Ph.D., 60 pp.

Overhead distribution systems in Thailand widely utilize space aerial cables (SAC) in many areas for improving system reliability. A common issue that has often been encountered in SAC systems is the damage of the insulation of the core conductor at spacer positions. One of the possible causes of this problem may be the occurrence of the partial discharge due to high electric field stress at the contact point between the cable and spacer. This thesis studies the electric field intensification near a contact point, at which the contact angle is zero, in a configuration of an insulated cylindrical conductor lying on a dielectric solid. In this configuration, the insulated conductor and the dielectric solid represent the SAC and spacer, respectively. The objectives of this thesis are first to determine the relationships between the degree of field intensification and the configuration parameters. In particular, the parameters are the geometric ratio of the thickness of the dielectric solid to the outer radius of the conductor insulation and the mismatch between the dielectric constants of the media involved. Then, the variation of the electric field at the contact point will be investigated in configurations in which a dielectric or conducting layer is inserted between the insulated conductor and the dielectric solid in order to mitigate the electric field intensification. In the analysis, the electric field is calculated analytically by using the method of multipole images in two dimensions to realize high accuracy.

Department : Electrical Engineering   Student's Signature ....

Field of Study : Electrical Engineering   Advisor's Signature ....

Academic Year : 2010

Acknowledgements

First of all, I would like to take this opportunity to express my deepest gratitude to my thesis supervisor, Associate Professor Boonchai Techaumnat, for all his careful guidance and considerable support during my study at Chulalongkorn University. This thesis would not have been possible without his great encouragement and enthusiastic supervision. My sincere thanks are also sent to Professor Kunihiko Hidaka for his advices and supports. I greatly acknowledge the actual data from Provincial Electric Authority (PEA), Thailand for my thesis.

I am thankful to Chulalongkorn University, especially the High Voltage Laboratory, for making an excellent and professional working environment. I am indebted to Associate Professor Boonchai Techaumnat, Assistant Professor Komson Petcharaks, Dr. Channarong Banmongkol, Dr. Weerapun Rungseevijitprapa, Assistant Professor Kulyos Audomvongseree, Dr. Surachai Chaitusaney, Professor David Banjerdpongchai and Assistant Professor Suchin Arunsawatwong, for proving me the fundamental background involving the field of Power Systems. The knowledge that I gained from their lectures is particularly useful not only for the work in this thesis but also for my future research.

I greatly appreciate the considerable effort of all the committee members including Associate Professor Boonchai Techaumnat, Assistant Professor Komson Petcharaks, Dr. Channarong Banmongkol and Dr. Aphibul Pruksanubal who have spent time in reading the manuscript of the thesis and attending the thesis defence. Their useful comments and constructive advices are absolutely invaluable. I am indebted to Assistant Professor Komson Petcharaks for his advice on the floating conductor. My thanks also go to everyone at Chulalongkorn University, especially students and staffs of High Voltage Laboratory, for their great friendship and enthusiastic help.

I gratefully acknowledge the full financial support from the ASEAN University Network/Southeast Asia Engineering Education Development Network (AUN/SEED-Net) for my Master's program in Thailand. My sincere thanks are also extended to the International School of Engineering (ISE), Chulalongkorn University for their care and help during my study.

Finally, I would like to dedicate this thesis to all members in my family for their endless love and support.

Contents

Page

List of Tables

List of Figures

Figure Page

List of Notations

Symbols

Φ complex potential

V_0 potential applied to core conductor

E_0 external field from other phase conductor

R_C inner radius of core conductor

R outer radius of conductor insulation

D_S thickness of dielectric solid

ε_A dielectric constant of surrounding air

ε_I dielectric constant of conductor insulation

ε_S dielectric constant of dielectric solid

E_c electric field at contact point with presence of dielectric solid

E_{c1} electric field at contact point without dielectric solid

CHAPTER I

INTRODUCTION

1.1 Introduction

Overhead lines are usually used in transmission and distribution systems. Typical overhead lines are bare conductors with sufficient spacing for insulation by the atmospheric air. However, in Thailand, overhead distribution systems widely utilize covered conductors in many areas for improving reliability of the systems. The covered conductors, called “space aerial cable (SAC)” in Thailand, consist of aluminium as the main conductor, semi-conductive shield, cross-linked polyethylene (XLPE) as the main cable insulation, and the cable jacket as shown in Figure 1.1.

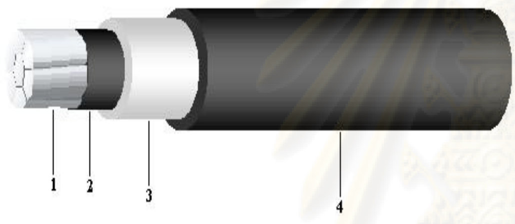

1. Conductor (aluminium)
2. Conductor shield (semi-conductive XLPE)
3. Insulation (XLPE)
4. Jacket (black XLPE)

Figure 1.1: Structure of space aerial cable [1].

By using SAC, we can reduce the distance required between the phase conductors and prevent faults due to incidental contact by other conductors or trees. Still, the cable cannot be in direct contact with grounded potential as the insulation of the SAC is not designed for the full system voltage. For both mechanical and electrical separation, various kinds of cable supporters, such as spacers and post-type insulators, are required in the overhead-line systems. The cable spacer currently in use with the SAC overhead distribution lines by the provincial electric authority (PEA), Thailand, can be classified into two categories: (1) porcelain spacer and (2) high-density polyethylene (HDPE) spacer.

A number of problems have been encountered in the systems of SAC overhead lines after a period of service. For the lines installed with HDPE spacers, the problems are mostly related to mechanical strength of the spacers and to tracking on their surface. In addition, the deterioration of the cable insulation was found at the contact position between the cable and spacer, in particular where the porcelain spacers are used [2]. In worst cases, the damage of the cable insulation led to flashover between phase conductors. As a result from the flashover, the line conductor and/or the spacer were broken, interrupting the electric power distribution.

One of the possible causes of the problem on the cable insulation may be the occurrence of partial discharge due to high electric field at the contact point between the cable and the spacer. The contact point is a triple junction formed by three dielectrics: the cable insulation, the spacer and the surrounding air, as schematically shown in Figure 1.2. The contact angle is zero by the curved contour of the conductor insulation as to be mentioned in the section 1.2. Therefore, it is necessary to study electric field behavior near the contact point.

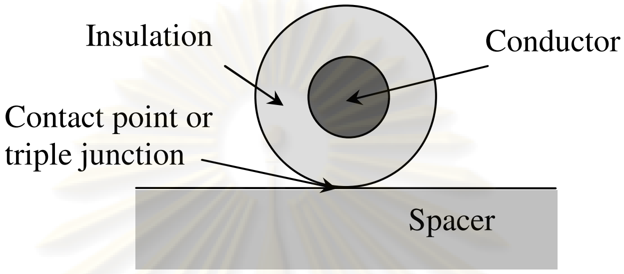

Figure 1.2: Covered conductor on a spacer.

1.2 Literature Review

A triple junction or a contact point is a point where three media meet together and exists in many insulation systems. For instance, it may be formed by a dielectric solid utilized as a mechanical support of an electrode or by a particle resting on an electrode, in which the electrode can be either bare or insulated conductor. The contact conditions are basically characterized by a contact angle α. Based on the electric field behavior, we can classify the contact points into three categories as follows: (1) $\alpha = 90°$, (2) $0 < \alpha < 90°$ and (3) $\alpha = 0°$. Figure 1.3 gives an illustration of contact points in fundamental cases where the interface of two dielectrics ε_1 and ε_2, meets a conductor surface. It should be noted that the contact conditions as illustrated in Figure 1.3 may be used to represent both two-dimensional (2D) and axisymmetrical (AS) arrangements. For Figure 1.3c, the contact angle is zero due to a smooth contact. That is, the interfaces have a common tangent at the contact point.

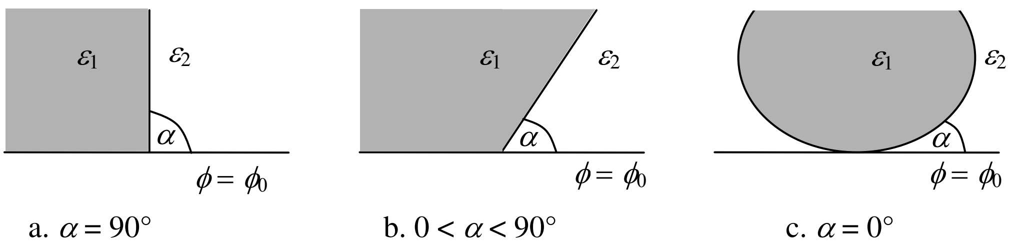

Figure 1.3: Contact conditions with various contact angles α.

Near the contact point, the distribution of electric field is important and is of interest, as the field is often significantly intensified here. The high field stress possibly causes partial discharge or inception of breakdown phenomenon within the insulation system. There were many publications on the electric field at triple junction by using both analytical and numerical methods. Such as the publications reported by T. Takuma and B. Techaumnat [3–6], the electric field at a triple junction usually exhibits complicated behavior. The field heavily depends on the contact angle and the electrical properties of the involved media. The field behavior at the contact point is basically summarized according to α as follows: First, for $\alpha = 90°$, the field may be enhanced by a certain degree but still finite. Second, for $0 < \alpha < 90°$, the field is either zero or infinity, which depends on the involved media. Finally, for $\alpha = 0°$, the field is finite but possibly much more intensified than that in the first category.

Up to now, the electric field behavior at the zero-angle contact point has been extensively investigated [4, 7–9]. The investigations treat a variety of interface shapes near the contact point such as a circle and a non-circle, and the effects of conductivity in the media. However, the focus is mainly on the cases in which one of the involved media is a conductor. For example, a dielectric particle is between parallel-plate conductors, a spheroid or an elliptic cylinder resting on conducting plane under external electric field, etc. In these cases, the field strength is always maximal at the point of contact and can be significantly intensified with increasing the dielectric constant of the dielectric media. Near the contact point, the field distribution becomes more nonuniform. In the investigated configurations, there is a configuration similar to that in Figure 1.2 has been studied [9].

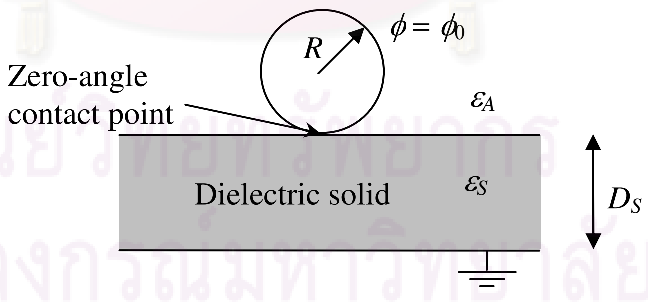

Figure 1.4: Bare cylindrical conductor lying on a dielectric solid.

As shown in Figure 1.4, the configuration is a bare cylindrical conductor of radius R in contact with a dielectric solid of finite thickness D_S and dielectric constant ε_S. The background medium is air with dielectric constant ε_A. In this case, the contact angle is zero but the media are a conductor and two dielectrics. The electric field is calculated by using the charge simulation method, a numerical method. The results of calculation show that the maximum field at the contact point is significantly intensified by either increasing of dielectric constant ε_S or decreasing of thickness D_S.

On the other hand, the electric field behavior at a contact point formed by three dielectrics was also reported by Takuma's group in [6, 9–12]. The electric field has been studied mainly for the contact angles between 0 and 90°, i.e., non-zero contact angle. The field strength approaches a singular or zero value at the contact point. Near the contact point, the field varies as a function of r^{n-1} where r is the distance from the contact point to calculating point and n is positive smaller than unity. The value of n is used to evaluate the enhancement of the field strength near the contact point. Principally, it depends on the electrical and geometrical parameters of configuration. Besides, the value of n cannot be given in a closed form, but obtained by using appropriate numerical methods such as the Newton-Raphson method.

1.3 Objectives

The purposes of this thesis are to study the electric field behavior near the triple junction between three dielectrics where the contact angle is zero, and to investigate approaches for reducing the intensification of electric field at the junction.

1.4 Scope of Thesis

This study is confined to a simplified configuration in which the covered-conductor cable is modeled as a coaxial cylinder with a single layer of insulation in most cases. The cable lies on a dielectric solid of finite thickness. The dielectric constants of typical polyethylene (PE) and porcelain are applied in the analysis. All these media, except the conductor, are assumed to be perfect dielectric. The electric field is calculated by using an analytical method of mutipole images in two dimensions.

1.5 Thesis Outline

The contents of the thesis are organized as follows:

Chapter II generally presents the method of multipole images in two dimensions, which is applied to the electric field calculations. Three image schemes related to configuration of the thesis such as that of grounded plane, dielectric plane and coaxial cylinders are also considered.

Chapter III explains the calculation results for the electric field behavior near the contact point in configuration of an insulated conductor resting on a dielectric solid of finite thickness. In addition, this chapter explains the influences from other phase conductors on the field distribution.

Chapter IV discusses three techniques of field mitigation at the contact point. The techniques focus on the insertion of a dielectric or a conducting layer between the conductor insulation and the dielectric solid.

Chapter V gives the conclusions of the thesis.

CHAPTER II

METHOD OF MULTIPOLE IMAGES

2.1 Introduction

This thesis applies the method of multipole images for two dimensions to the electric field analysis in the configuration of Figure 1.2. The multipole images such as monopole, dipole and quadrupole are utilized to represent charges in the arrangement. For example, Figure 2.1 illustrates the physical interpretation of a 2D monopole and a 2D dipole, respectively, as a line charge and two closely-spaced parallel line charges of equal magnitudes but opposite polarities.

a) Monopole

b) Dipole

Figure 2.1: Physical interpretation of a monopole and a dipole in space.

The method of multipole images is an analytical method whose principle is to insert appropriate multipole charge images in order to satisfy all boundary conditions in the configuration. The determination of the magnitude and the position of the images are based on the image schemes of fundamental arrangements such as the scheme of a grounded plane or that of dielectric cylinders. Hence, the application of this method is limited to configurations which are composed of simpler arrangements with the available image schemes. However, this method has an advantage over numerical methods, as high accuracy of calculation results can be realized, particularly for the configuration under consideration here which involves curved boundary contours.

Note that the presence of mutipole images in this method may cause a numerical problem in calculation. As we know that, at an infinitely far position from a source charge, the potential due to a 2D monopole (line charge) is singular, whereas that due to other 2D multipoles vanishes. This characteristic leads to numerical instability when applying the multipole re-expansion which is to be discussed later in the section 2.3, although the relations are theoretically correct. Besides, the potential by a monopole is a function of natural logarithm, i.e., $\ln(r)$, where r is the distance from the source. Thus, a reference potential (zero potential) is taken at an arbitrary point.

We may here let the point be at a unit radius for simplicity. By such reference of zero potential, the potential of a monopole decreases from infinity to zero as the distance r increases from zero to unity. Therefore, I solve the numerical problem by restricting the spatial dimensions of the calculation arrangements to be smaller than unity. An arrangement with larger dimension is scaled down so as to conform to this restriction. However, when a very small value of r combined with a high order of multipoles may give a numerical overflow of the potential.

2.2 Expression of the Potential

For this method, a complex plane $z = x + iy$ is used to represent a two-dimensional physical space. The real and imaginary parts describe geometrically the abscissa and the ordinate of a point (x, y) in the physical space. From the complex theory [13], a function $\Phi = \phi + i\psi$ is analytic only if it satisfies the two Cauchy-Riemann equations:

$$\frac{\partial\phi}{\partial x} = \frac{\partial\psi}{\partial y} \text{ and } \frac{\partial\phi}{\partial y} = -\frac{\partial\psi}{\partial x}. \tag{2.1}$$

The real and imaginary parts of the analytic function Φ satisfy Laplace's equation. That is

$$\nabla^2\phi = \frac{\partial^2\phi}{\partial x^2} + \frac{\partial^2\phi}{\partial y^2} = 0 \text{ and } \nabla^2\psi = \frac{\partial^2\psi}{\partial x^2} + \frac{\partial^2\psi}{\partial y^2} = 0. \tag{2.2}$$

I here call Φ the complex potential and choose the real part ϕ as the real potential.

Consider a complex plane as shown in Figure 2.2, in which a number of sources (line charges) exist. q_i and q_j are respectively denoted as the charges inside the inner circle $|z - z_0| = r_1$ and outside the outer circle $|z - z_0| = r_2$. These circles have the same center at z_0. For a region defined by $r_1 \le |z - z_0| \le r_2$, the complex potential due to q_i and q_j can be expressed in a general form as a sum of two infinite series expanded about z_0:

$$\Phi = \Phi_B + \Phi_L, \tag{2.3}$$

where Φ_B is the potential of multipoles,

$$\Phi_B = B_0 \ln(z - z_0) + \sum_{n=1}^{\infty} \frac{B_n}{(z - z_0)^n}; \tag{2.4}$$

and Φ_L is the potential of Taylor expansion or local expansion,

$$\Phi_L = \sum_{n=0}^{\infty} L_n (z - z_0)^n \ . \qquad (2.5)$$

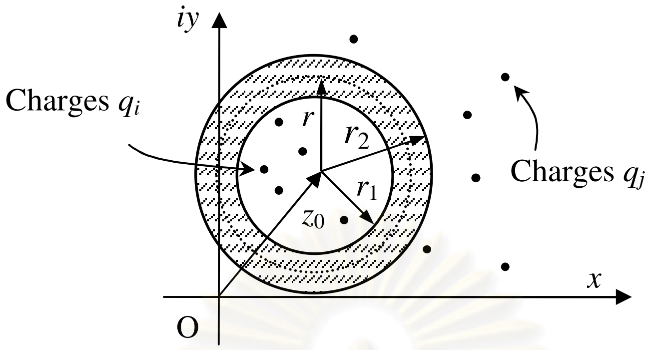

Figure 2.2: Region $r_1 \le |z - z_0| \le r_2$. Charges q_i are inside the circle of radius r_1, and charges q_j are outside the circle of radius r_2.

Φ_B is the potential due to all charges q_i, whereas Φ_L is the potential due to all charges q_j. Note that in (2.4) Φ_B is singular at z_0. The potential coefficients B_n and L_n are complex numbers, which are to be determined in the calculation to fulfill the boundary conditions involved. For example, if a line charge with charge density q_0 is located at (x_0, y_0) in a medium of permittivity of ε, then the charge is presented by a monopole or zero-order multipole $B_0 = -q_0/2\pi\varepsilon$ at z_0 in the complex plane.

2.3 Re-expansion of Complex Potential

For the multipole image method, three types of re-expansion of the complex potential are often utilized as a combination to makes possibly the application of the method for various arrangements. I here use the term "re-expansion" for the processes that expand the function Φ about a different center in a form of multipole potential in (2.4) or a form of local expansion in (2.5). Actually, the processes are done based on expansion of Maclaurin series through a dimension ratio smaller than unity. Therefore, the series with a high order of expansion are applied to reduce errors appeared in the expansion process. Details of expansion formulas as well as their proofs are described in [13–15].

In this section, I present briefly two types of the re-expansion which are used for this thesis. The first type only translates the center of expansion in form of multipole potential (without change in the form of expression), whereas the last one not only translates the center of expansion but also rewrites the multipole potential into the form of local expansion.

2.3.1 Translation of multipole expansion

Consider an nth-order multipole B_n at $z_0 = x_0 + iy_0$ in a complex plane, as shown in Figure 2.3. Such as (2.4), at any position z in the complex plane, the complex potential Φ_{B_n} due to this multipole is equal to $B_0 \ln(z - z_0)$ for $n = 0$ and $B_n/(z - z_0)^n$ for $n \geq 1$. However, with the center of expansion moved to the origin O, we can re-expand Φ_{B_n} for region $|z| > |z_0|$, i.e., outside the circle of radius z_0 and center O. The potential is expressed as

$$\Phi_{B_n} = \sum_{j=n}^{\infty} \Phi_{C_j}\,, \tag{2.6}$$

where C_j are the multipoles located at O. That is, $\Phi_{C_0} = C_0 \ln z$ and $\Phi_{C_j} = C_j / z^j$. The new multipoles, C_j with $j \geq n$, are determined from the original B_n as follows:

If $n = 0$,

$$C_0 = B_0\,, \tag{2.7}$$

$$C_j = -\frac{z_0^j B_0}{j} \qquad (j \geq 1). \tag{2.8}$$

If $n \geq 1$,

$$C_j = z_0^{j-n} \frac{(j-1)!}{(j-n)!(n-1)!} B_n \qquad (j = n, n+1, \ldots). \tag{2.9}$$

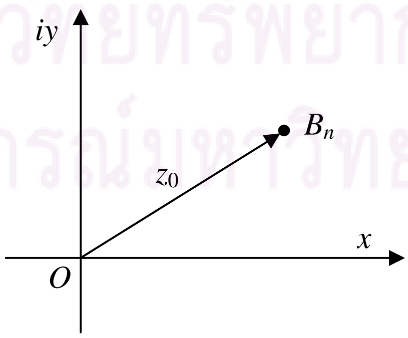

Figure 2.3: Multipole B_n at z_0 in the complex plane.

2.3.2 Conversion from multipole expansion to local expansion

Consider the same multipole in Figure 2.3. For the region $|z| < |z_0|$, i.e., inside the circle of radius z_0 and center O, we can express the complex potential Φ_{B_n} in the form of local expansion as the center of expansion moved to the origin O. The potential is rewritten as

$$\Phi_{B_n} = \sum_{j=0}^{\infty} \Phi_{M_j} , \tag{2.10}$$

where M_j (j = 0, 1, ...) are the potential coefficients of the re-expansion. That is, $\Phi_{M_j} = M_j z^j$ for $j \geq 0$. We can determine M_j from B_n as follows:

If $n = 0$,

$$M_0 = \ln(-z_0)B_0 \quad (j = 0), \tag{2.11}$$

$$M_j = -\frac{B_0}{j z_0^j} \quad (j \geq 1). \tag{2.12}$$

If $n \geq 1$,

$$M_0 = \frac{B_n}{(-z_0)^n} \quad (j = 0), \tag{2.13}$$

$$M_j = (-1)^n \frac{B_n}{z_0^{n+j}} \frac{(j+n-1)!}{j!(n-1)!} \quad (j \geq 1). \tag{2.14}$$

2.4 Calculation of the Electric Field

After the complex potential are already determined, the electric field of E_x and E_y in x and y directions at any point in the space are calculated from the complex potential Φ as follows:

$$E_x = -\frac{\partial \phi}{\partial x} = -\frac{\partial \operatorname{Re}(\Phi)}{\partial x} = -\frac{\operatorname{Re}(\partial \Phi)}{\partial x} \text{ and} \tag{2.15}$$

$$E_y = -\frac{\partial \phi}{\partial y} = -\frac{\partial \operatorname{Re}(\Phi)}{\partial y} = \frac{\operatorname{Im}(\partial \Phi)}{\partial x}. \tag{2.16}$$

Since
$$\frac{\partial \Phi}{\partial z} = \frac{\partial \operatorname{Re}(\Phi)}{\partial x} + i\frac{\partial \operatorname{Im}(\Phi)}{\partial x}, \tag{2.17}$$

the magnitude of electric field is expressed as

$$E = \left| \frac{\partial \Phi}{\partial z} \right|. \tag{2.18}$$

2.5 Image Schemes

Like the conventional image method, determination of position and magnitude of multipole images is the first step and is the fundamental of the calculation. As the configuration in Figure 1.2 is complicated, the multipole images cannot be directly established to fulfill all involved boundary conditions in one time. Thus, image schemes of simpler arrangements, which compose the configuration, are utilized. This section presents the image schemes of three fundamental arrangements: grounded plane, dielectric plane and coaxial cylinders. Multipole images from the image schemes are applied to the calculation in an iterative manner, and the calculation is terminated when the change in the maximum electric field at the contact point from that in the previous repetition is smaller than 10^{-4}%. The highest order of the multipoles in the calculation is as high as 60. After the multipole images are obtained, the potential and electric field can be determined by using (2.3) and (2.18), respectively.

2.5.1 Grounded plane

Multipole B_n is at $z_0 = x_0 + iy_0$ above a grounded plane as shown in Figure 2.4. Charges are induced on the grounded plane. To determine the potential above the grounded plane, we replace all the induced charges by an image multipole $B_n^{'}$ at the conjugate $\overline{z}_0 = x_0 - iy_0$. $B_n^{'}$ is calculated as:

$$B_n^{'} = -\overline{B}_n \quad \text{for } n \geq 0. \tag{2.19}$$

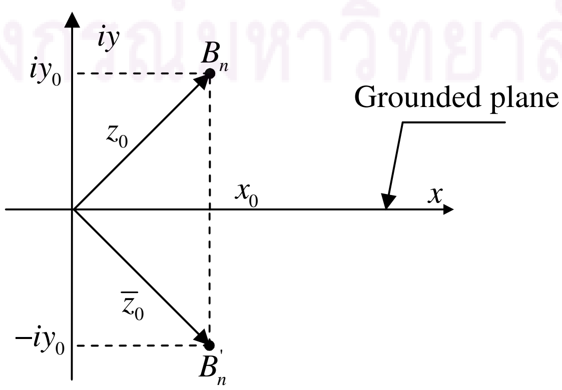

Figure 2.4: Image $B_n^{'}$ induced by grounded plane from source multipole B_n.

2.5.2 Dielectric plane

Figure 2.5 shows a configuration of a multipole B_n placed at $z_0 = x_0 + iy_0$ above a dielectric plane. For this configuration, two multipole images, $B_n^{'}$ placed at $\overline{z}_0$ and $B_n^{''}$ at z_0, are used to satisfy the boundary conditions at $y = 0$. The potential above the dielectric plane is the sum of potentials caused by B_n and $B_n^{'}$, whereas the potential below the dielectric plane is the potential due to $B_n^{''}$. $B_n^{'}$ and $B_n^{''}$ can be calculated as follows (for $n \geq 0$):

$$B_n^{'} = -\frac{\Gamma - 1}{\Gamma + 1}\overline{B}_n \quad \text{and} \tag{2.20}$$

$$B_n^{''} = \frac{2}{\Gamma + 1}B_n, \tag{2.21}$$

where the permittivity ratio $\Gamma = \varepsilon_2 / \varepsilon_1$.

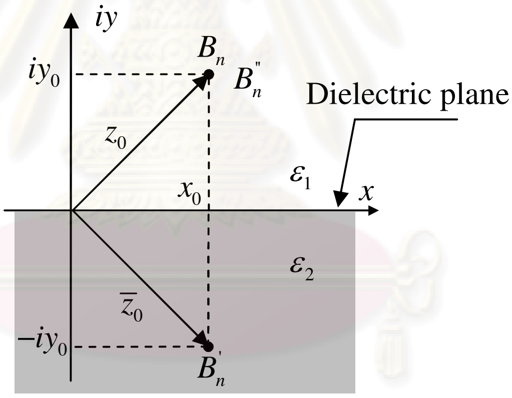

Figure 2.5: Images $B_n^{'}$ and $B_n^{''}$ induced by dielectric plane from source multipole B_n.

2.5.3 Coaxial cylinders

In this section, two cases of potential sources are considered for the arrangement of coaxial cylinders. That is, (i) a fixed potential V_0 at the inner cylinder and (ii) a multipole B_n outside the coaxial cylinders. They are respectively shown in Figures 2.6 and 2.7. The coaxial cylinders are composed of an inner conductor with radius R_C and an outer dielectric layer, called the conductor insulation, with radius R. I denote the dielectric constants (relative permittivities) of the dielectric layer and that of the surrounding medium by ε_1 and ε_2, respectively. The surfaces of the conductor and conductor insulation are represented by terms “Boundary 1” and “Boundary 2”, respectively. In both cases (i) and (ii), charges are induced on both Boundary 1 and Boundary 2. In order to satisfy boundary conditions on the boundaries, we utilize three multipole images whose complex potential is expanded at center of the cylinders.

i. Potential V_0 at the inner conductor

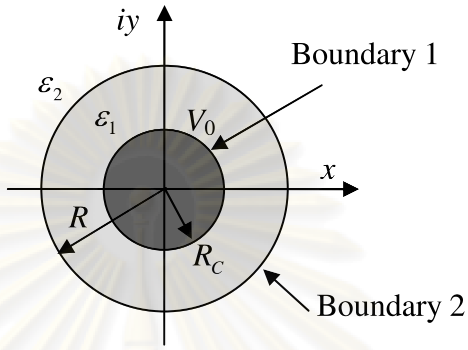

Figure 2.6: Fixed potential V_0 at inner coaxial conductor.

First, for a fixed potential at the conductor as in Figure 2.6, the charges on the conductor are presented by a monopole or zero-order multipole image. Hence, there exists only monopole component in added images. Then, the potential (Φ_{in}) inside the conductor insulation, $R_C \le |z| \le R$, and (Φ_{out}) outside the conductor insulation, $z \ge R$, are calculated as

$$\Phi_{in} = \Phi_{C_0} + \Phi_{L_0} = C_0 \ln z + L_0 \text{ and} \tag{2.22}$$

$$\Phi_{out} = \Phi_{D_0} = D_0 \ln z , \tag{2.23}$$

where Φ_{C_0} and Φ_{L_0} are the monopole potential due to the charges on the conductor surface and the induced charges on the surface of conductor insulation in determining potential inside the conductor insulation, respectively. Φ_{D_0} is the monopole potential resulted from the charges on both Boundaries 1 and 2 for calculating potential outside the cylinders.

Based on fulfilling boundary conditions, the following equations are used to compute the magnitude of monopole images, where $\Gamma = \varepsilon_1 / \varepsilon_2$:

$$C_0 = \frac{V_0}{\ln R_C + (\Gamma - 1)\ln R} , \tag{2.24}$$

$$L_0 = \frac{(\Gamma - 1)\ln R}{\ln R_C + (\Gamma - 1)\ln R} V_0 , \tag{2.25}$$

$$D_0 = \frac{\Gamma}{\ln R_C + (\Gamma - 1)\ln R} V_0 . \tag{2.26}$$

In this case, if the coaxial cylinders are covered by a floating conductor layer at the radius R, then it is required one more boundary condition of equipotential at R. However, as the potential is constant anywhere on Boundary 2 by (2.24)–(2.26). The presence of the floating conductor does not have any influence on the calculation of image to fulfill the condition of potential V_0. That is, the equations from (2.22) to (2.26) are still applied.

ii. A multipole B_n outside the cylinders

Consider the second arrangement of a multipole B_n outside the coaxial cylinders as in Figure 2.7. In this case, as the potential source V_0 is replaced by source B_n, the potential at the conductor must be vanished by connecting to zero potential.

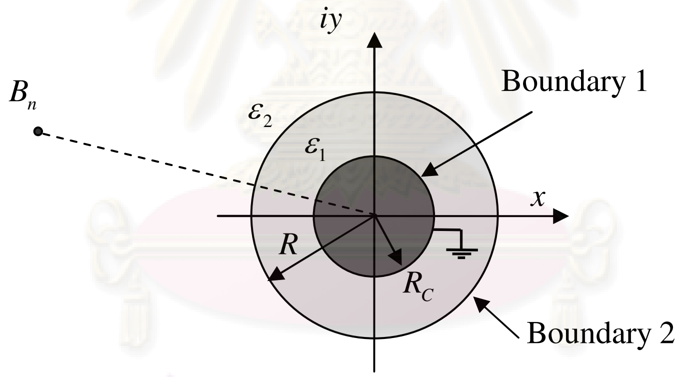

Figure 2.7: Multipole B_n located outside coaxial cylinders.

First of all, we utilize a re-expansion formula in (2.10) to re-expand the complex potential due to the external sources of B_n to local expansion form about center of the cylinders for simplicity. Thus, the inserted images include both monopole and multipole components. The center of the cylinders is treated as the origin. Then, for multipole B_n, the potential (Φ_{in}) inside the conductor insulation, $R_C \le |z| \le R$, is described as

$$\Phi_{in} = \Phi_{C_j} + \Phi_{L_j} = \left[C_0 \ln z + \sum_{j=1}^{\infty} \frac{C_j}{z^j} \right] + \left[\sum_{j=0}^{\infty} L_j z^j \right], \tag{2.27}$$

and the potential (Φ_{out}) outside the conductor insulation, $z \geq R$, is expressed as

$$\Phi_{out} = \Phi_{B_n} + \Phi_{D_j} = \left[\sum_{j=0}^{\infty} M_j z^j\right] + \left[D_0 \ln z + \sum_{j=1}^{\infty} \frac{D_j}{z^j}\right]. \tag{2.28}$$

In (2.27), the potential Φ_{C_j} is the multipole potential contributed from charges on the conductor surface, whereas Φ_{L_j} is the multipole potential of B_n and induced charges on the outer surface of the conductor insulation. In (2.28), Φ_{D_j} is the multipole potential representing induced charges on both Boundaries 1 and 2 for calculating potential outside the cylinders.

From the boundary conditions, the magnitude of multipole images is determined as follows:

For $j = 0$,

$$C_0 = -\frac{1}{(\Gamma - 1)\ln R + \ln R_C} \mathrm{Re}\{M_0\}, \tag{2.29}$$

$$L_0 = \frac{\ln R_C}{(\Gamma - 1)\ln R + \ln R_C} \mathrm{Re}\{M_0\}, \tag{2.30}$$

$$D_0 = -\frac{\Gamma}{(\Gamma - 1)\ln R + \ln R_C} \mathrm{Re}\{M_0\}. \tag{2.31}$$

For $j \geq 1$,

$$B_j = -\frac{2R_C^{2j}}{(\Gamma+1) + (\Gamma-1)\left(R_C/R\right)^{2j}} \overline{M_j}, \tag{2.32}$$

$$L_j = \frac{2}{(\Gamma+1) + (\Gamma-1)\left(R_C/R\right)^{2j}} M_j, \tag{2.33}$$

$$D_j = \left\{\frac{2\left[1 - \left(R_C/R\right)^{2j}\right]}{(\Gamma+1) + (\Gamma-1)\left(R_C/R\right)^{2j}} - 1\right\} R^{2j} \overline{M_j}. \tag{2.34}$$

When the coaxial cylinders are covered a floating conductor layer at the radius R, the application of the images and calculation process is slightly changed as follows: For monopole component j = 0, the equations from (2.29) to (2.31) are still applied here. For higher-order multipole components $j \geq 1$, the multipole images C_j and L_j, which are utilized for calculating potential inside the conductor insulation, do not exist. That is,

$$C_j = L_j = 0\,. \tag{2.35}$$

Besides, as the surface of the conductor insulation is a floating conductor, we apply the formula derived in [16] to mutipole image D_j as

$$D_j = -R^{2j}\overline{M_j}\,. \tag{2.36}$$

2.6 Examples of Calculation Process

This section presents some examples of the application of the multipole image method to field calculation in 2D configurations. The configurations are formed as the combination of simple arrangements explained in Section 2.5.

2.6.1 Grounded plane and dielectric plane

Figure 2.8 shows a source multipole B_n and its images with respect to two Boundaries 1 and 2. B_n is at a distance d above Boundary 1 on y axis of the (x, y) coordinate system (see Figure 2.8). Boundary 1 is an interface of two dielectric media **a** and **b** having dielectric constants ε_a and ε_b, respectively. Boundary 2 is a grounded plane. The thickness of medium **b** is D.

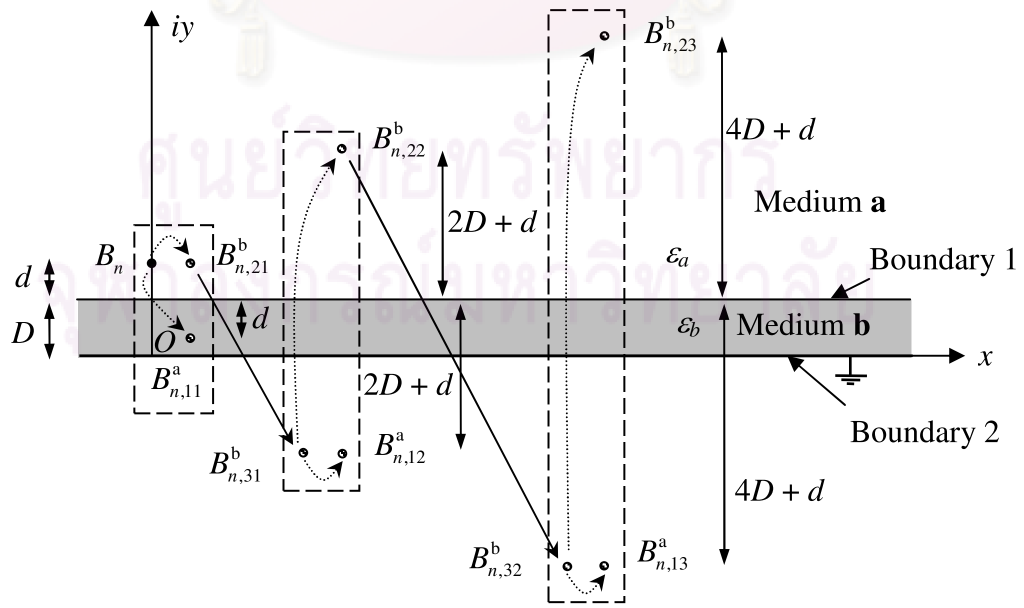

Figure 2.8: Multipole images inserted to satisfy boundary conditions of grounded plane and dielectric plane from multipole B_n.

Note that all inserted images and the source B_n lie on the same vertical line (i.e., on the y axis). However, the positions of images are at different x coordinate to clearly illustrate the sequence of image insertion. In the expression of the images, for example, $B^{\mathrm{a}}_{n,11}$, then the superscript "a" indicates the medium for which the image is used to calculate the potential, and the subscript "11" is associated with the image position. The images in Figure 2.8 are inserted sequentially to satisfy boundary conditions on Boundaries 1 and 2, as presented in the flowchart in Figure 2.9.

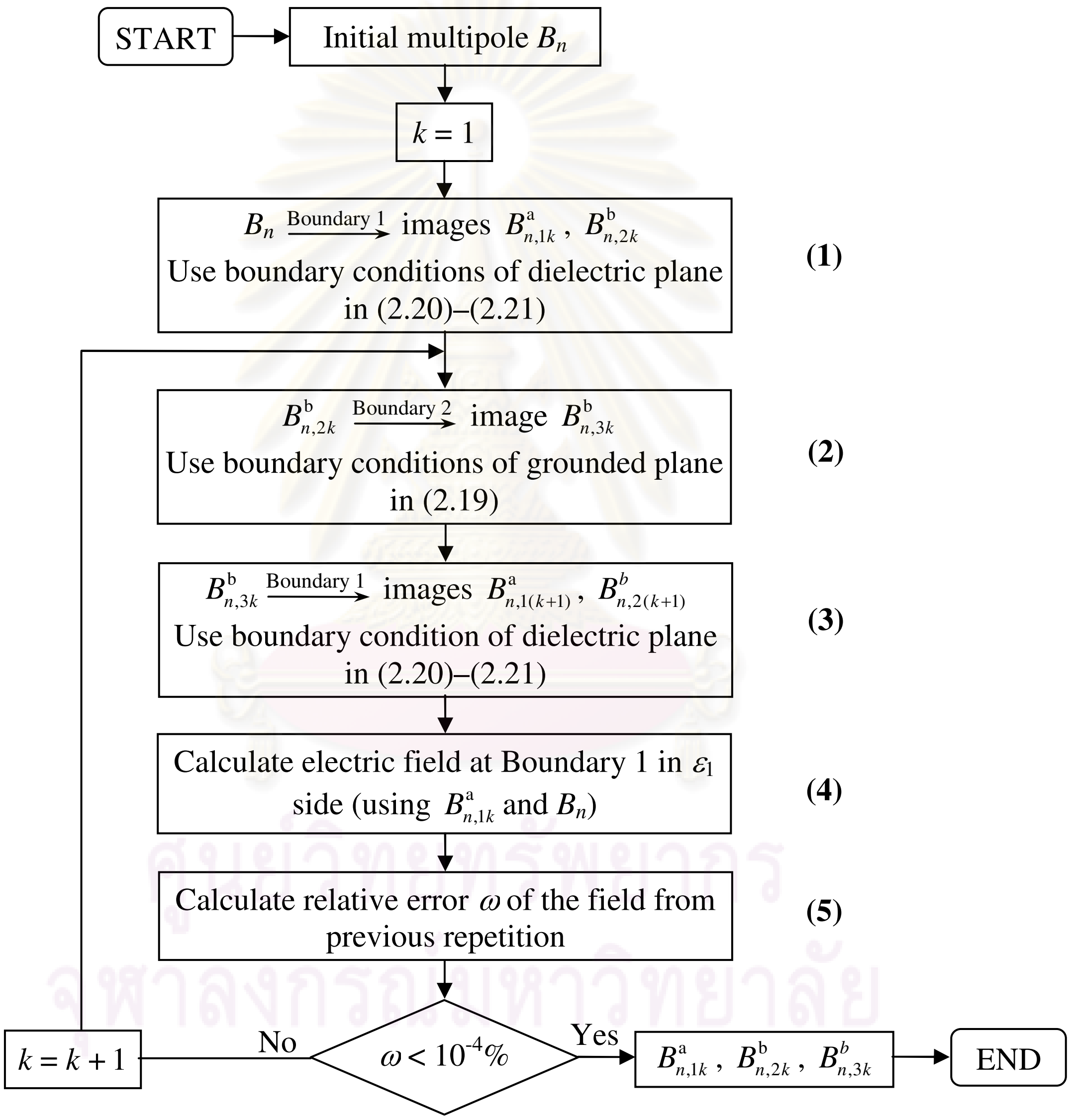

Figure 2.9: Flowchart for insertion of images $B^{\mathrm{a}}_{n,1k}$, $B^{\mathrm{b}}_{n,2k}$ and $B^{\mathrm{b}}_{n,3k}$ from multipole B_n.

For instance, with step k = 1, at **(1)** we use two images $B^{\mathrm{a}}_{n,11}$ at $z_{11} = (D-d)i$ and $B^{\mathrm{b}}_{n,21}$ at $z_{21} = (D+d)i$ to fulfill conditions on Boundary 1 by the multiople B_n. Magnitudes of these images are computed by using (2.20) and (2.21), where $\Gamma = \varepsilon_b/\varepsilon_a$:

$$B^{\mathrm{a}}_{n,11} = -\frac{\Gamma-1}{\Gamma+1}\overline{B}_n \text{ and } B^{\mathrm{b}}_{n,21} = \frac{2}{\Gamma+1}B_n . \tag{2.37}$$

In **(2)**, from the image $B^{\mathrm{b}}_{n,21}$, an image $B^{\mathrm{b}}_{n,31}$ at $z_{31} = \left[D-\left(d+2D\right)\right]i$ is inserted for condition on Boundary 2. Its magnitude is determined by (2.19) as

$$B^{\mathrm{b}}_{n,31} = -\overline{B^{\mathrm{b}}_{n,21}} . \tag{2.38}$$

Then in **(3)**, the appearance of $B^{\mathrm{b}}_{n,31}$ disrupts boundary conditions on Boundary 1 that is established in Step 1. Hence, two images $B^{\mathrm{a}}_{n,12}$ at $z_{12} = \left[D-\left(d+2D\right)\right]i$ and $B^{\mathrm{b}}_{n,22}$ at $z_{22} = \left[D+\left(d+2D\right)\right]i$ are utilized to satisfy conditions on Boundary 1 from $B^{\mathrm{b}}_{n,31}$. The equations (2.20) and (2.21) are also applied to their magnitude calculation:

$$B^{\mathrm{a}}_{n,12} = \frac{2\Gamma}{\Gamma+1}B^{\mathrm{b}}_{n,31} \text{ and } B^{\mathrm{b}}_{n,22} = \frac{\Gamma-1}{\Gamma+1}\overline{B^{\mathrm{b}}_{n,31}} . \tag{2.39}$$

Theoretically, an infinite number of images are needed to completely fulfill the boundary conditions. However, we may truncate the calculation after m steps when the influences of the newly added images become negligible. These images can be classified into three categories of $B^{\mathrm{a}}_{n,1k}$, $B^{\mathrm{b}}_{n,2k}$ and $B^{\mathrm{b}}_{n,3k}$ whose magnitudes are presented in Table 2.1. These categories are respectively characterized by position groups of z_{1k}, z_{2k} and z_{3k}. In particular,

$$z_{1k} = \left[D-\left(d+2(k-1)D\right)\right]i , \tag{2.40}$$

$$z_{2k} = \left[D+\left(d+2(k-1)D\right)\right]i , \tag{2.41}$$

$$z_{3k} = \left[D-\left(d+2kD\right)\right]i . \tag{2.42}$$

where k = 1, 2, 3 …

Table 2.1: Magnitudes of image groups $B^{\mathrm{a}}_{n,1k}$, $B^{\mathrm{b}}_{n,2k}$ and $B^{\mathrm{b}}_{n,3k}$.

Images	$k = 1$	$k = 2$	$k = 3$	…	$k = m$ (only $m \geq 2$)
$B^{\mathrm{a}}_{n,1k}$	$-\frac{\Gamma-1}{\Gamma+1}\overline{B_n}$	$-\frac{4\Gamma}{(\Gamma+1)^2}\overline{B_n}$	$-\frac{4\Gamma(\Gamma-1)}{(\Gamma+1)^3}\overline{B_n}$	…	$-\frac{4\Gamma(\Gamma-1)^{m-2}}{(\Gamma+1)^m}\overline{B_n}$
$B^{\mathrm{b}}_{n,2k}$	$\frac{2}{\Gamma+1}B_n$	$-\frac{2(\Gamma-1)}{(\Gamma+1)^2}B_n$	$-\frac{2(\Gamma-1)^2}{(\Gamma+1)^3}B_n$	…	$-\frac{2(\Gamma-1)^{m-1}}{(\Gamma+1)^m}B_n$
$B^{\mathrm{b}}_{n,3k}$	$-\frac{2}{\Gamma+1}\overline{B_n}$	$\frac{2(\Gamma-1)}{(\Gamma+1)^2}\overline{B_n}$	$\frac{2(\Gamma-1)^2}{(\Gamma+1)^3}\overline{B_n}$	…	$\frac{2(\Gamma-1)^{m-1}}{(\Gamma+1)^m}\overline{B_n}$

Now we have already determined the magnitudes and the positions of all images. Then the equations (2.3) and (2.18) are applied to calculation of potential and electric field, respectively. For the medium **a**, we use the images $B^{\mathrm{a}}_{n,1k}$ and the multipole B_n, whereas the images $B^{\mathrm{b}}_{n,2k}$ and $B^{\mathrm{b}}_{n,3k}$ are utilized for the medium **b**.

2.6.2 Grounded plane, dielectric plane and coaxial cylinders

This section explains the calculation procedure for the configuration of coaxial cylinders and a dielectric sheet in a background medium, as shown in Figure 2.10. Three dielectrics in this figure are media **a**, **b** and **c** having dielectric constants ε_a, ε_b and ε_c, respectively. The inner cylinder is a conductor. The conductor is charged to potential V_0 and has radius R_1. The outer radius of the cylinders is R_2. The dielectric sheet has thickness D. This configuration may be applied to Section 3.2 and as a basic for other configurations in this thesis.

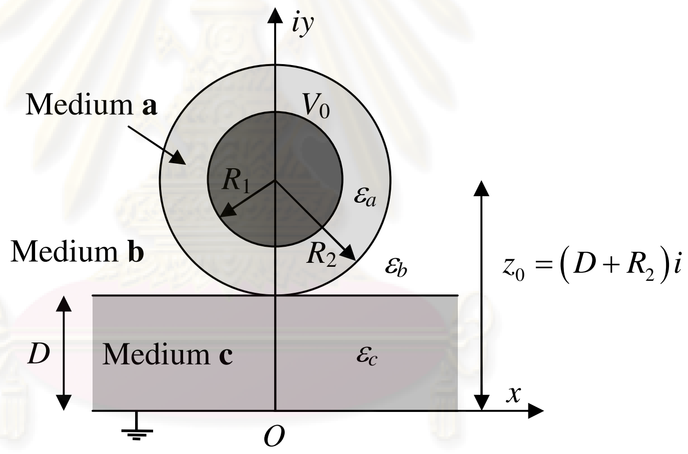

Figure 2.10: Configuration composed of coaxial cylinders and a dielectric sheet.

For the purpose of field calculation inside three dielectric media, we first need to determine the magnitudes and the positions of multipole images. Due to the complication of Figure 2.10, the configuration is subdivided into simpler objects, i.e., coaxial cylinders in Section 2.5.3 and dielectric sheet (including grounded plane and dielectric plane) in Section 2.6.1. The inserted images are determined by fulfilling boundary conditions of these objects. Figure 2.11 shows the flowchart for the insertion of multipole images. Note that the meaning of symbols enclosed images in the flowchart is similar to that in Section 2.6.1. Beside, the subscript letter "*j*" indicates the *j*-th step of the iteration. When a (x, y) coordinate system is assumed as in Figure 2.10, the center of the cylinders is at $z_0 = (D + R_2)i$.

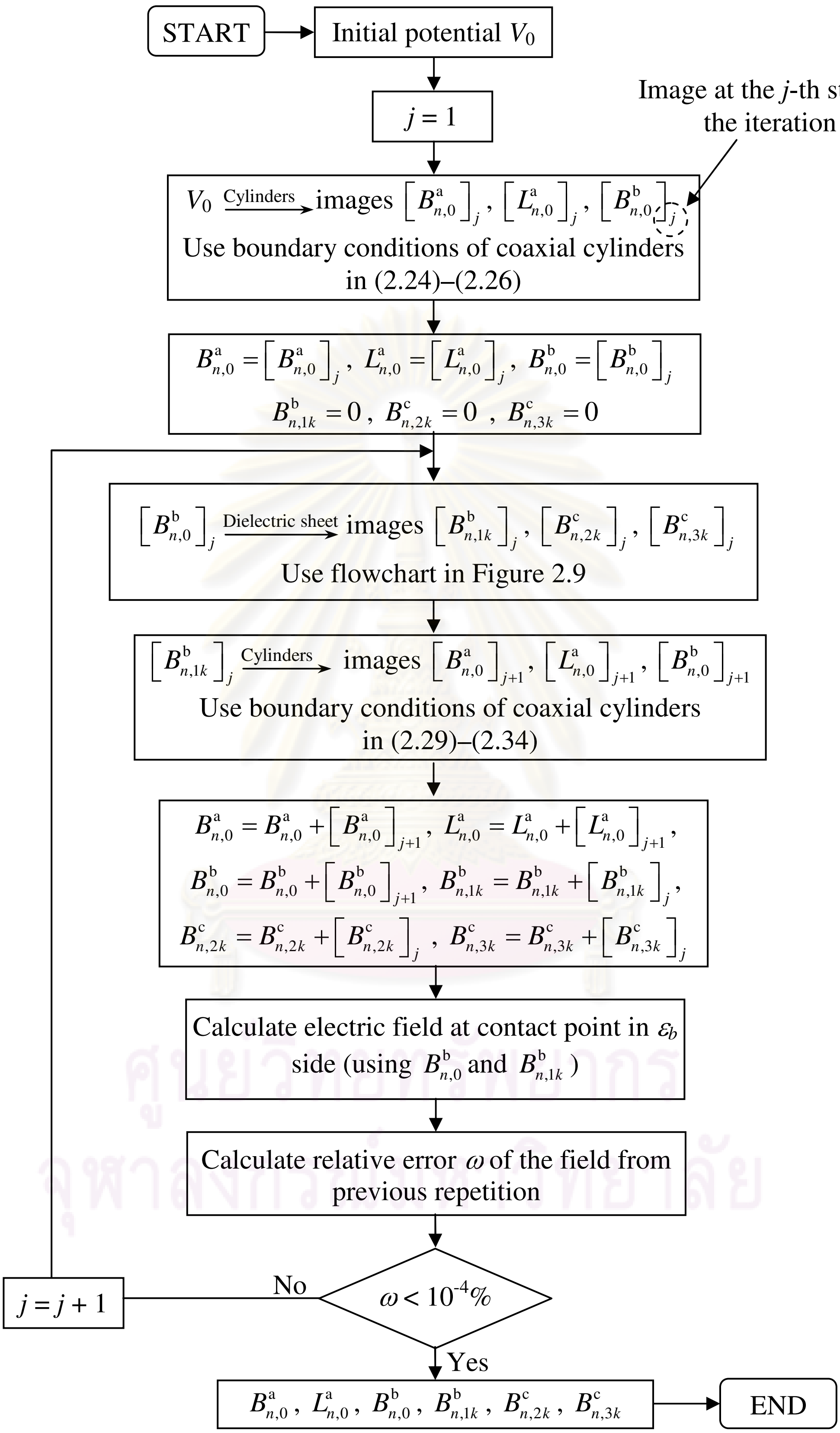

Figure 2.11: Flowchart for insertion of multiople images from of potential V_0.

The flowchart in Figure 2.11 can be explained briefly for step j = 1 as follows:

First, with an initial potential V_0 at the conductor, we use three images $\left[B_{n,0}^{\mathrm{a}}\right]_1$, $\left[L_{n,0}^{\mathrm{a}}\right]_1$ and $\left[B_{n,0}^{\mathrm{b}}\right]_1$ that is at the center of the coaxial cylinders z_0 to satisfy conditions of boundaries on the cylinders. Magnitudes of these images are calculated by using (2.24)-(2.26).

Then, the image $\left[B_{n,0}^{\mathrm{b}}\right]_1$ looks like placed in the medium **b** above the dielectric sheet a distance R_2. Hence, in order to fulfill two boundaries on the dielectric sheet, we utilize three image groups $\left[B_{n,1k}^{\mathrm{b}}\right]_1$, $\left[B_{n,2k}^{\mathrm{c}}\right]_1$ and $\left[B_{n,3k}^{\mathrm{c}}\right]_1$ whose positions are at z_{1k}, z_{2k}, and z_{3k}. Their magnitudes are related to $\left[B_{n,0}^{\mathrm{b}}\right]_1$ as shown in the Table 2.1, whereas the positions are computed by applying (2.40)-(2.42).

Next, the appearance of the images $\left[B_{n,1k}^{\mathrm{b}}\right]_1$ for the field calculation in the medium **b** disturbs the initial potential on the cylinders making the boundary conditions of the cylinders unsatisfied. Thus, we need three more images $\left[B_{n,0}^{\mathrm{a}}\right]_2$, $\left[L_{n,0}^{\mathrm{a}}\right]_2$ and $\left[B_{n,0}^{\mathrm{b}}\right]_2$ with respect to $\left[B_{n,1k}^{\mathrm{b}}\right]_1$ so as to satisfy the boundary conditions of the cylinders again. Equations (2.29)-(2.34) are applied to determine their magnitudes.

Now the image $\left[B_{n,0}^{\mathrm{b}}\right]_2$ is occurred again, which is similar to $\left[B_{n,0}^{\mathrm{a}}\right]_1$ in the first time. The new images will be inserted continuously in a similar process as explained above until the electric field caused by them is smaller than the desired relative error.

In the iterative process, the images which are the same kind (i.e., the same position) will be added together. For example, assuming that the number of iteration is fifty, we will have fifty images of $\left[B_{n,0}^{\mathrm{a}}\right]_j$, where j = 1, 2 … , 50. However, with additional process, finally there exists only one image $B_{n,0}^{\mathrm{a}}$, where $B_{n,0}^{\mathrm{a}} = \sum_{j=1}^{50}\left[B_{n,0}^{\mathrm{a}}\right]_j$.

Therefore, when the iteration is terminated, we have three images $B_{n,0}^{\mathrm{a}}$, $L_{n,0}^{\mathrm{a}}$, $B_{n,0}^{\mathrm{b}}$ at z_0 and three group images of $B_{n,1k}^{\mathrm{b}}$, $B_{n,2k}^{\mathrm{c}}$, $B_{n,3k}^{\mathrm{c}}$ at z_{1k}, z_{2k}, z_{3k}, respectively. For the calculation of potential and electric field, we utilize the images of $B_{n,0}^{\mathrm{a}}$ and $L_{n,0}^{\mathrm{a}}$ for the medium **a**, the images of $B_{n,0}^{\mathrm{b}}$ and $B_{n,1k}^{\mathrm{b}}$ for the medium **b**, and the images of $B_{n,2k}^{\mathrm{c}}$ and $B_{n,3k}^{\mathrm{c}}$ for the medium **c**. Note that the image $L_{n,0}^{\mathrm{a}}$ has potential in form of local expansion in (2.5), whereas all other images have potential in form of multipole in (2.4)

CHAPTER III

ELECTRIC FIELD BEHAVIOR NEAR THE CONTACT POINT

This chapter presents the analytical results of the electric field in a configuration of an insulated cylindrical conductor lying on a dielectric solid of finite thickness. The insulated conductor and dielectric solid represent a space aerial cable (SAC) and a spacer, respectively. This chapter considers electric field from two sources. First, the field results from the applied potential at the core conductor of the cable. That is, the electric field is caused by its own phase conductor. Second, the configuration is subjected to an external electric field due to the other phase conductors.

3.1 Space Aerial Cables (SAC) and the Models

Figure 3.1 illustrates the structure of SAC. The cable is composed of four components: aluminium conductor, conductor shield, XLPE insulation and outer XLPE jacket. Table 3.1 presents typical dimensions of 50 mm^2 and 185 mm^2 SACs used for 22 and 33 kV systems by the provincial electric authority (PEA), Thailand [2].

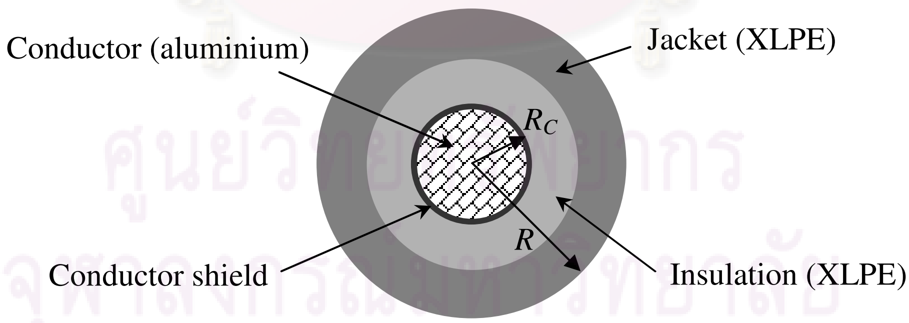

Figure 3.1: Cross-section model of aerial space cable.

Table 3.1: Dimension parameters of space aerial cables.

System voltage (kV)	Size (mm^2)	Diameter of conductor (mm)	Thickness of conductor shield (mm)	Thickness of insulation (XLPE) (mm)	Thickness of jacket (XLPE) (mm)
22	50	8.33	0.3	3.175	3.175
	185	15.98			
33	50	8.33		4.445	
	185	15.98			

For the purpose of field calculation, the SACs are modeled by using two coaxial cylinders so as to reduce the calculation complexity. The coaxial cylinders have core radius R_C including the conductor shield and total radius R including the jacket layer, as illustrated in Figure 3.1. The values of R_C and R are given in Table 3.2.

Table 3.2: Calculating parameters of various types of SAC.

System voltage (kV)	Size (mm^2)	Radius of conductor, R_C (mm)	Thickness of insulation layer (mm)	Outer radius of cable, R (mm)	R_C/R
22	50	4.465	6.35	10.815	0.4129
	185	8.29		14.64	0.5663
33	50	4.465	7.62	12.085	0.3695
	185	8.29		15.91	0.5211

From Table 3.2, the thickness $R–R_C$ of the insulation layer is the same for the cables for each system voltage, whereas R_C is independent for the system voltage. Note that R_C is increased by 1.86 times as the cable size increases from 50 mm^2 to 185 mm^2. The thickness $R–R_C$ increases 1.2 times as the system voltage increases from 22 to 33 kV (1.5 times).

3.2 Electric Field by the Phase Conductor

3.2.1 Configuration

A two-dimensional configuration of an insulated cylindrical conductor resting on a dielectric solid shown in Figure 3.2 is utilized for the study. As explained in Section 3.1, the insulated conductor represents the SAC, and the dielectric solid represents the cable spacer. The conductor has radius R_C and the outer radius of the cylinder is R. The thickness of the dielectric solid is D_S. The cylinder makes a contact with the dielectric solid at the point J, and the contact angle is zero at J due to the rounded contour of the conductor insulation.

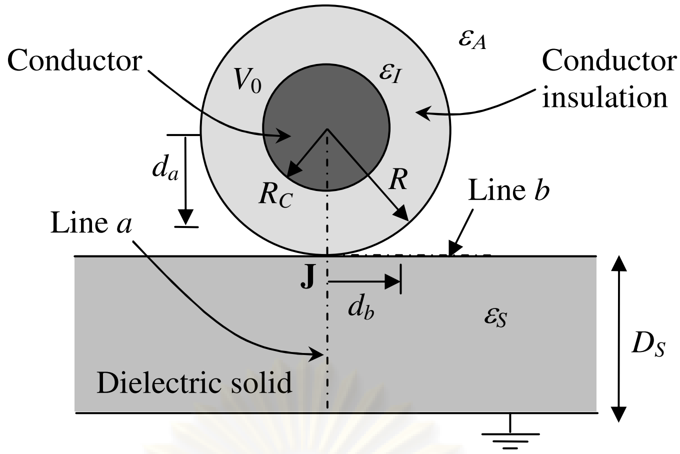

Figure 3.2: Insulated cylindrical conductor lying on a dielectric solid.

For the study of electric field by the potential of the insulated conductor, the conductor is charged at potential V_0 and a grounded potential is assumed at the lower surface of the dielectric solid. The dielectric constants of the conductor insulation and the dielectric solid are denoted by ε_I and ε_S, respectively, whereas unit dielectric constant ε_A is used for the surrounding medium (air).

In this section, the focus is on the relationships between the degree of field intensification and the configuration parameters, in particular, (i) the ratio of the thickness D_S to the outer radius R of the cylinder and (ii) the mismatch between the dielectric constants ε_S and ε_I. I consider the system voltages of 22 and 33 kV, i.e., $V_0 = 22\sqrt{2}/\sqrt{3}$ and $33\sqrt{2}/\sqrt{3}$ kV. The radius ratios R_C/R according to the values in Table 3.2 are used to reflect the practical SACs. That is,

- $R_C/R = 0.4129$ for SAC 50 mm^2 used for 22 kV,
- $R_C/R = 0.5663$ for SAC 185 mm^2 used for 22 kV,
- $R_C/R = 0.3695$ for SAC 50 mm^2 used for 33 kV,
- $R_C/R = 0.5211$ for SAC 185 mm^2 used for 33 kV.

The spacer thickness D_S between $0.001R$ and $10000R$ is used to study its influence on the electric field. This range of D_S covers all cases in practice.

The insulation material of the SAC is cross-linked polyethylene (XLPE). Therefore, $\varepsilon_I = 2.2$ is applied to the calculation. The dielectric solid (spacer) is usually made from high-density polyethylene (HDPE) or porcelain. In this thesis, the dielectric constant ε_S of the dielectric solid is varied from 1 to 7 to investigate its effects on the electric field. This range of ε_S includes the values 2.2 for HDPE and 7 for porcelain. The case $\varepsilon_S = 1.5$, which does not really exist, is also treated because I want to know how the electric field changes when the dielectric constant of the dielectric solid is lower than that of HDPE. HDPE is a material having the lowest dielectric constant in materials used for the spacer at present.

3.2.2 Electric field distribution

This section presents electric field distribution near the contact point J in Figure 3.2. The field is considered on Line *a* and Line *b* shown in Figure 3.2. Line *a* is a vertical line starting from the center of the conductor through the contact point to the lower surface of the dielectric solid. The position of a point on this line is indicated by the distance d_a measured from the center of the conductor. This means that $d_a/R = R_C/R$ corresponds to the conductor surface. The field on Line *a* has only downward vertical component because of the symmetry of the configuration. Line *b* is a horizontal line along the upper surface of the dielectric solid. The position of a point on Line *b* is indicated by the distance d_b measured from J. This means that $d_b/R = 0$ represents the contact point.

In the following results, the size of SAC and system voltage are denoted by A-B, where A is the size of SAC and B is the system voltage. For example, SAC50-22kV is applied to case of SAC 50 mm^2 used for 22 kV systems.

The field distribution is presented here as an example for the cases of $D_S/R = 1$ and $\varepsilon_S = 1$, 2.2 and 7. The calculation results are obtained by the method of multipole images. Figures 3.3 and 3.4 show the typical distribution of the electric field on Line *a* and Line *b*. Notice that the field values are taken on the ε_A (air) side for Line *b*.

It is clear from Figure 3.3 that the characteristic of the electric field is governed by ε_S. The field characteristics are similar for all the system voltage and cable sizes. The electric field strength is maximal at the conductor surface for all cases of ε_S. The field usually decreases with increasing distance from the conductor. However, in the case of $\varepsilon_S = 7$, the field becomes stronger with increasing d_a near the contact point. In the dielectric solid, the maximum field strength is always at the contact point, and higher for lower ε_S.

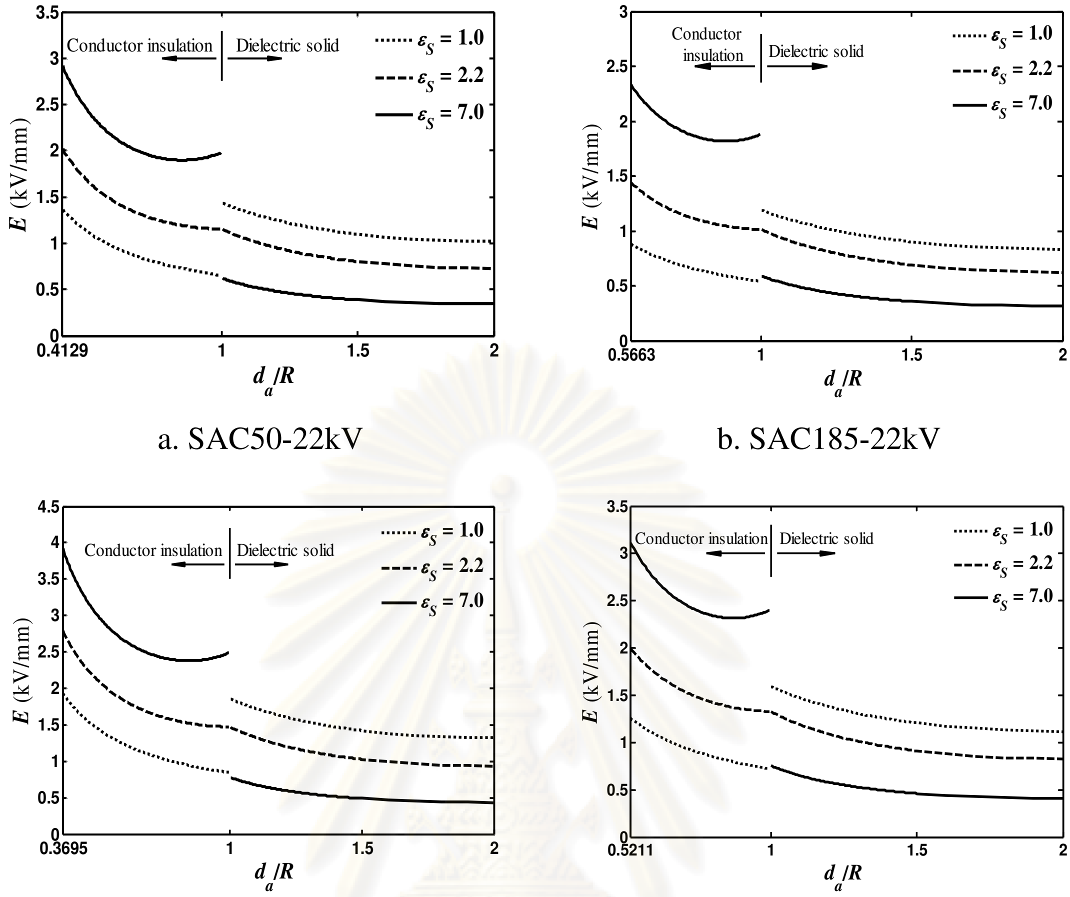

a. SAC50-22kV
b. SAC185-22kV
c. SAC50-33kV
d. SAC185-33kV

Figure 3.3: Magnitude of electric field from the phase potential on Line *a* for the case of $D_S/R = 1$.

In Figure 3.4, the electric field is plotted as a function of the normalized distance d_b/R. The field distributions are similar to each other for all cases of system voltages and cable sizes. The field is maximal at the contact point and decreases with increasing distance from J. Higher values ε_S always yield stronger electric field at any positions considered in Figure 3.4. Therefore, this figure clearly shows the intensification of the electric field in the air side by ε_S. In addition, in comparison with the field magnitudes in Figure 3.3, we can see that the maximum field in the configuration occurs at the contact point J in the air side.

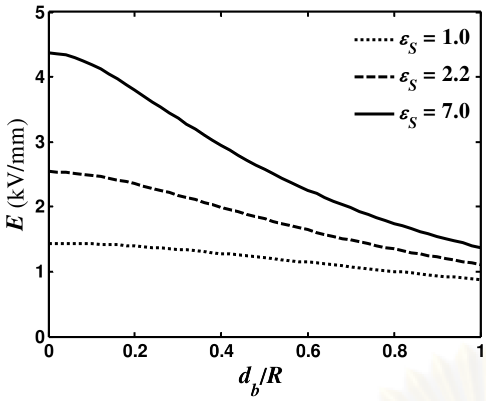

a. SAC50-22kV

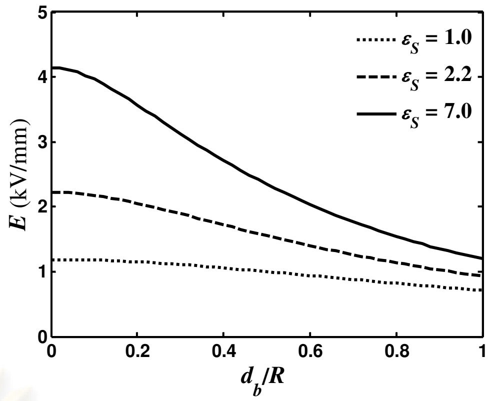

b. SAC185-22kV

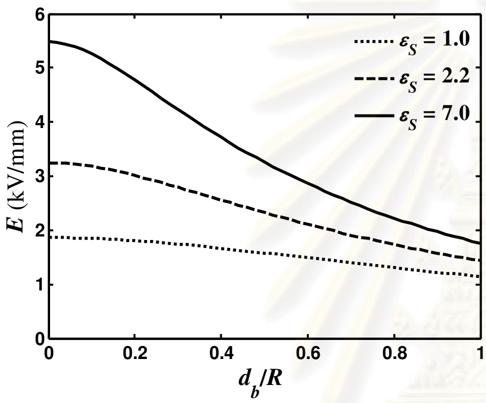

c. SAC50-33kV

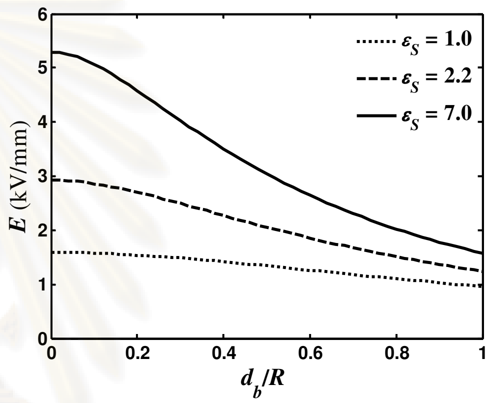

d. SAC185-33kV

Figure 3.4: Magnitude of electric field from the phase potential on Line *b* for the case of $D_S/R = 1$.

When comparing the field strength at the contact point in Figures 3.4, it can be seen that the field strength has a small difference and the difference is larger for higher ε_S. In particular, for $\varepsilon_S = 7$, with increasing the system voltage (compare Figures 3.4a to c, and Figures 3.4b and d.), the field strength increases up to 1.25 times for SAC 50 mm^2 and 1.28 for SAC 185 mm^2. Besides, with increasing the size of SAC (compare Figure 3.4a to b, and Figure 3.4c and d.), the field strength is almost unchanged for the same system voltage 22 kV and 33 kV.

3.2.3 Contact-point electric field

This section presents the intensification of electric field at the contact point in air side, as air is the medium with the lowest dielectric strength in the configuration and the field maximum takes place at the contact point in the air side. E_{c1} is defined as the maximum electric field at the contact point in air side without the dielectric solid (ε_S = 1). The field strength E_{c1} for four types of SAC is compared in Figure 3.5 as a function of D_S/R. We can see that E_{c1} for all the cable types behaves similarly with the change in D_S/R. That is, E_{c1} decreases with increasing D_S/R rather fast for D_S/R up to unity. With a further increase in D_S/R, the field decreases more slowly, but should approach a lower limit for $D_S/R = \infty$. However, with increasing the system voltage, E_{c1} becomes higher, especially for smaller D_S/R; and the cable size does not have a significant effect on E_{c1} as the field varies only slightly with the cable size in Figure 3.5.

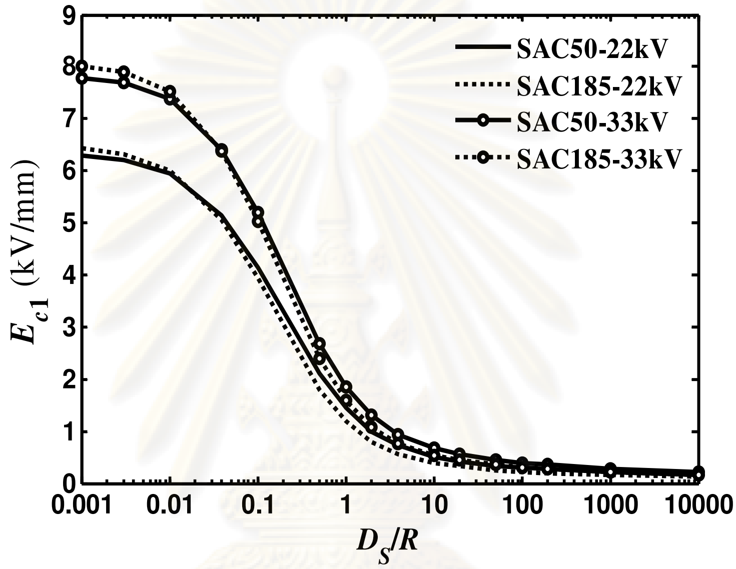

Figure 3.5: Electric field E_{c1} as a function of D_S/R.

With the presence of the dielectric solid, the electric field E_c at the contact point is always higher than E_{c1}. The ratio E_c/E_{c1}, considered as an index of the field intensification, is presented as a function of D_S/R in Figure 3.6a, b and c for three values of ε_S. Figure 3.6 demonstrates that all the types of SAC exhibit similar relationship between E_c/E_{c1} and D_S/R. The role of ε_S on the electric field intensification (E_c/E_{c1}) becomes predominantly with increasing D_S/R (although the field magnitude E_c decreases). For any ratio D_S/R, larger values ε_S result in higher E_c/E_{c1}.

As D_S/R increases, E_c/E_{c1} becomes higher; however, the saturation of E_c/E_{c1} can be seen in Figure 3.6 for ε_S = 1.5 and 2.2. The saturation value of E_c/E_{c1} depends on ε_S. For the case of SAC50-22kV, with large D_S/R = 1000, E_c/E_{c1} = 2.51 for ε_S = 2.2 (HDPE) and 7.88 for ε_S = 7 (porcelain). That is, in this case the electric field is stronger by 3.14 times or higher with porcelain than with HDPE as the lower dielectric constant.

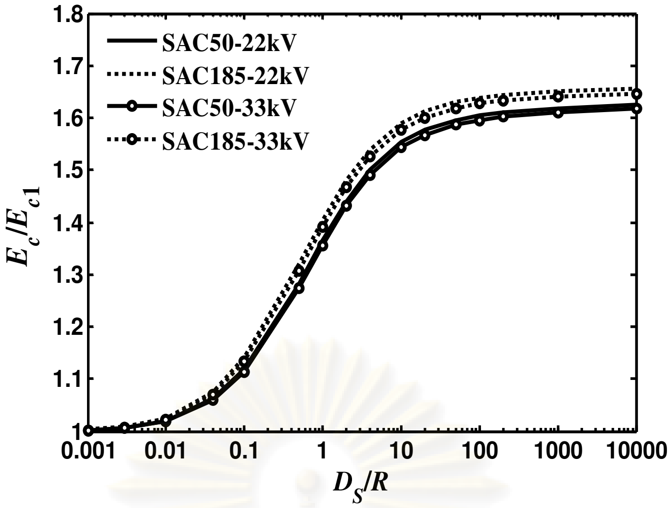

a. $\varepsilon_S = 1.5$

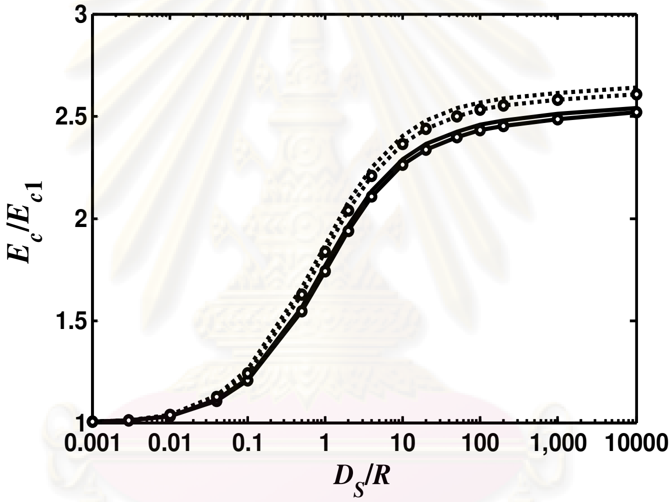

b. $\varepsilon_S = 2.2$

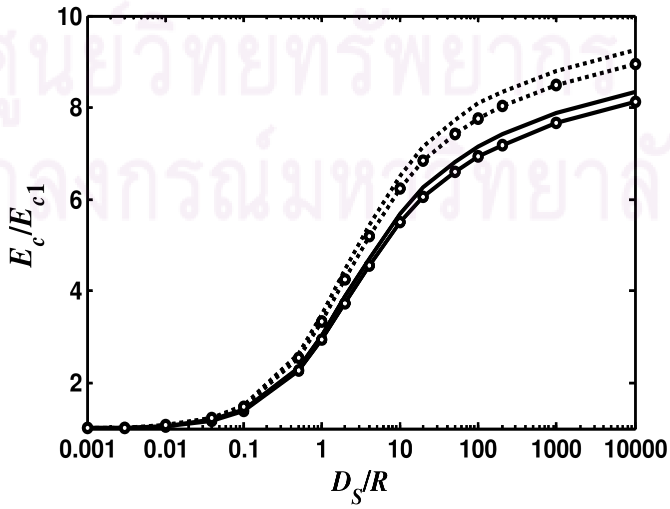

c. $\varepsilon_S = 7.0$

Figure 3.6: Field ratio E_c/E_{c1} as a function of D_S/R.

Figure 3.7 shows the difference $\Delta(E/E_{c1})$ of E_c/E_{c1} based on comparison with the E_c/E_{c1} of the type SAC50-22kV at the same D_S/R. The difference is given in percentage for ε_S = 2.2 and 7. It is clear that magnitude of $\Delta(E/E_{c1})$ increases with D_S/R from zero and reaches the maximum value at D_S equal to a few times of R. Compare Figures 3.7a to b, we can see that $\Delta(E/E_{c1})$ increases with ε_S. For example, with SAC185-22kV, the maximum difference is 5.87 % as ε_S = 2.2, whereas that equal to 15.15% as ε_S = 7. Besides, the difference according to SAC50-33kV is much smaller than that of SAC185-22kV. This means that the field ratio is less influenced by the system voltage than the cable size. This regard is opposite to the above remark about field strength in Figure 3.5.

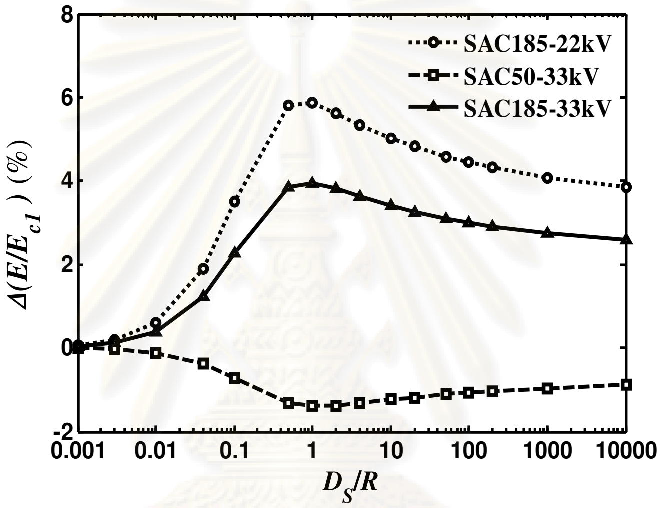

a. $\varepsilon_S = 2.2$

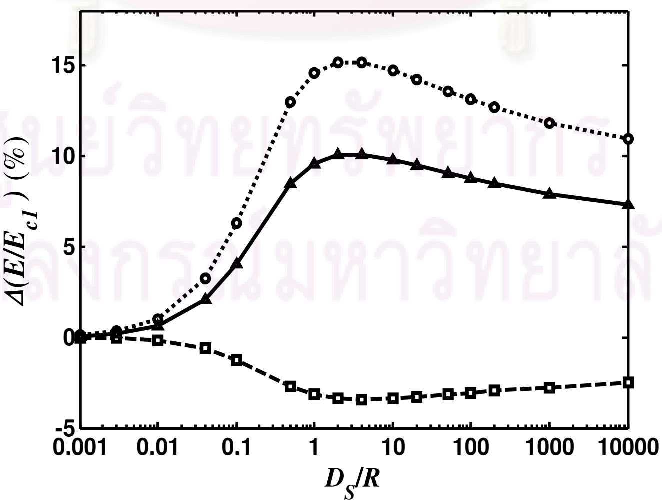

b. $\varepsilon_S = 7.0$

Figure 3.7: Difference of ratio E_c/E_{c1} in comparison with SAC50-22kV.

The electric field distribution has been analyzed for various types of SAC in the same configuration. Although the field strength and the field ratio vary between types of the SAC, their distributions are principal in the same form. Thus, the subsequent parts such as Section 3.3 and Chapter IV can be done only on the type of SAC50-22kV as a typical example. The values of the contact-point field strength and the field ratio E_c/E_{c1} are given in Appendix A.

For arrangements with zero-contact angle in composite dielectrics including gas medium, the electric field in the gas medium is intensified and can be considered as a quasi-uniform field in close vicinity of the contact point. Hence, apart from applying numerical and analytical methods, the field strength in the gas gap near the point of contact may be determined approximately by sharing the applied voltage between dielectric media at the contact point through capacitance impedances in series. This is a simple one which can be sometimes able to predict the field strength. Details of using the capacitance model to estimate the field strength near the contact point in air side for a typical case in Figure 3.2 are present in Appendix B.

Finally, Figure 3.8 shows the magnitude of electric field E_c at the contact point in the air side for the various types of SAC for cases of ε_S = 2.2 and 7. It is clear that E_c for all the cables types distributes similarly with change in D_S/R. Compare to Figure 3.5, the effect of the cable size and the system voltage on the field strength of E_c is same with that of E_{c1}.

Continued in the next page

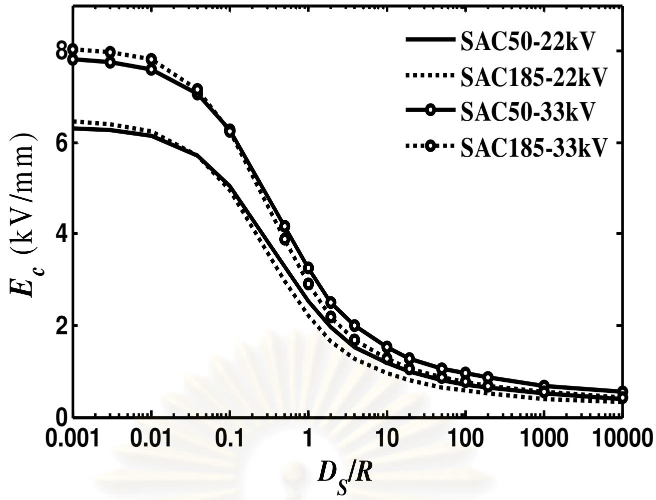

a. $\varepsilon_S = 2.2$

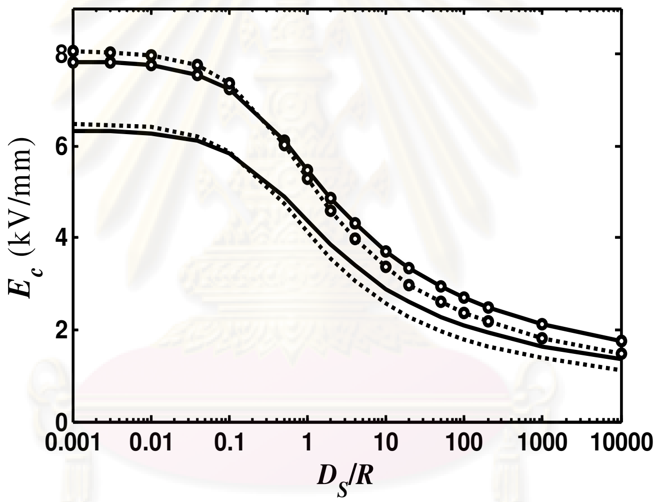

b. $\varepsilon_S = 7$

Figure 3.8: Magnitude of electric field E_c as a function of D_S/R.

3.3 Influences from the Other Phase Conductors

The previous section discusses the electric field due to the potential applied to the core conductor. However, the field at the contact is generated not only by the potential at phase conductor under consideration but also by the other phase conductors. The calculation of electric field by these two sources can be done perfectly independently. The superposition theory may then be applied to obtain the actual field.

In this section, I investigate the influences on the field distribution when the configuration of analysis is subjected to an external field. As the distance between phases is much larger than the dimension of the phase conductor, the external field may be treated as a uniform field.

3.3.1 Configuration

Figure 3.9 shows the configuration used to analyze the influence of an external field on the contact-point electric field. The configuration is similar to that in Figure 3.2. However, the external uniform field E_0 exists as the source. The core conductor is grounded to zero potential by the superposition theory, whereas no boundary condition is applied to the lower surface of the dielectric solid.

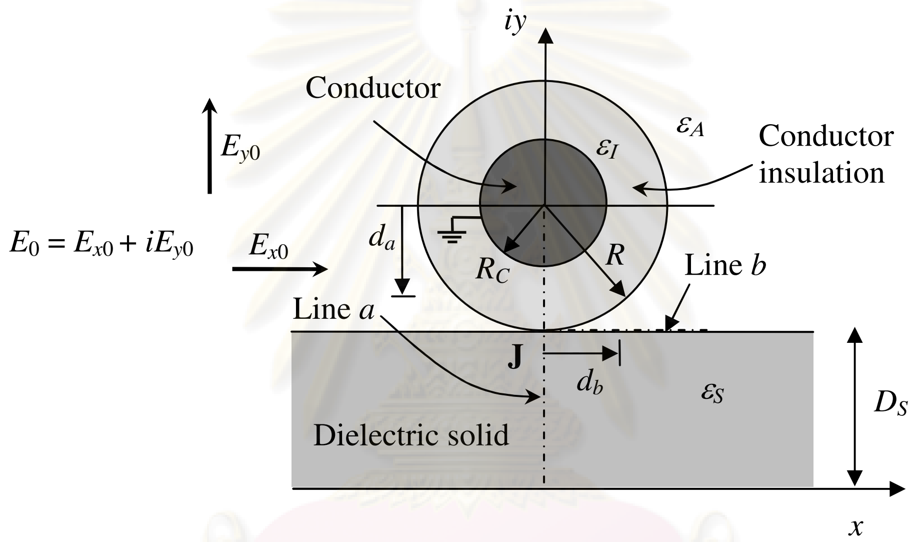

Figure 3.9: Configuration for analysis under an external uniform electric field.

As the configuration is symmetric with respect to the $x = 0$ plane, the component E_{x0} is not intensified at the contact point. This means that the field in horizontal direction at the contact point is equal to E_{x0}. Thus, this section considers only the external field E_{y0} in the vertical direction. The field calculation for the configuration in Figure 3.9 is carried out for the type of SAC 50 mm^2 used for 22 kV (refer to Table 3.2).

3.3.2 Electric field distribution

As a typical example, the field distribution in this section is carried out for case D_S/R = 1. Similar to the section 3.2.2, the electric field is considered on both Line *a* and Line *b* (see Figure 3.9). Figures 3.10 and 3.11 show the typical distribution of the electric field on Line a and Line b for cases of $D_S/R = 1$, and $\varepsilon_S = 1$, 2.2 and 7. The field magnitude is normalized by E_{y0}.

When comparing Figure 3.10 to Figure 3.3a and Figure 3.11 to Figure 3.4a, it demonstrates that the field distribution exhibits almost similarly. However, in Figure 3.10 the electric field in dielectric solid is more influenced by ε_S than that in the conductor insulation, and in Figure 3.11 the electric field is lower for higher ε_S as d_b/R is higher than about 0.75.

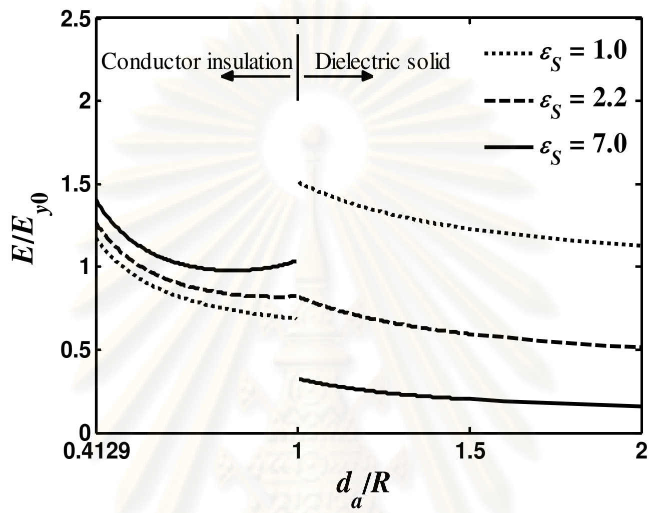

Figure 3.10: Magnitude of electric field from the external field on Line a for the case of $D_S/R = 1$.

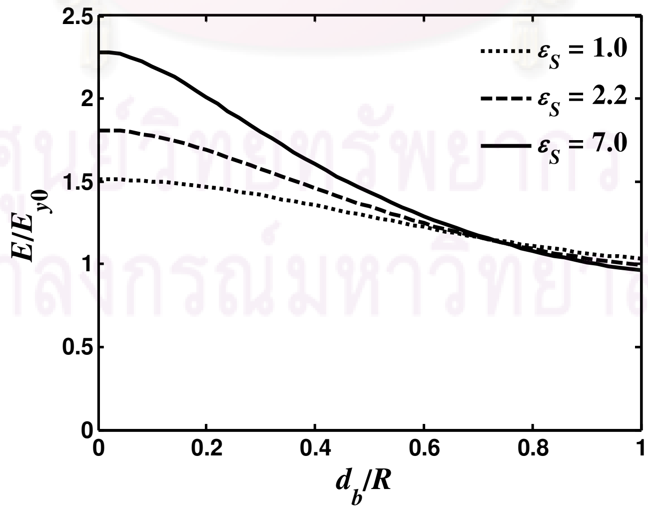

Figure 3.11: Magnitude of electric field from the external field on Line b for the case of $D_S/R = 1$.

3.3.3 Contact-point electric field

Under the external electric field, the electric field E_c at the contact point in air side is always higher than E_{y0}. The ratio E_c/E_{y0} is considered as an index of the field intensification. It should be noticed that the field by E_{y0} at J is only in upward vertical direction. Figures 3.12 shows the ratio E_c/E_{y0} for cases of ε_S = 1, 2.2 and 7 as D_S/R varied from 0.001 to 20. It is seen that the saturation of E_c/E_{y0} is taken as D_S/R approaches zero. As D_S/R increases, for ε_S = 1 the field ratio is not modify; whereas for ε_S = 2.2 and 7 it becomes higher and almost constant as $D_S/R \geq 1$. For any D_S/R, larger values ε_S result in higher E_c/E_{y0}. When D_S/R = 20 and ε_S = 7, E_c/E_{y0} = 2.4.

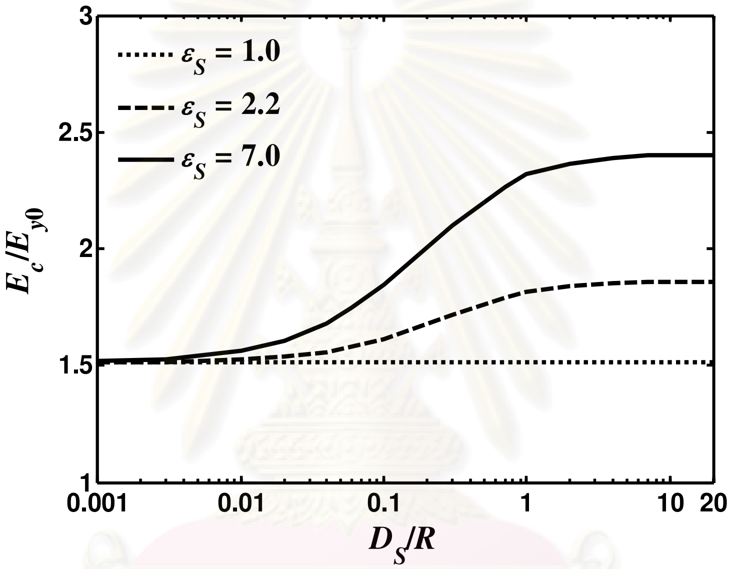

Figure 3.12: Field ratio E_c/E_{y0} as a function of D_S/R.

As we know that the electric field by line charges decreases as function of $1/r$, where r is distance from the source, in homogeneous medium. The distance from the contact point under consideration to the potential source at the other phase conductors is much larger than that to the potential source at the own phase conductor. Thus, the influence of the other phase conductors on the field at the contact point under consideration is negligible. In particular, the external field E_0 is approximately 1000 times smaller than the electric field caused by the own phase conductor, which is referred to Appendix C. Besides, the results shown in Figure 3.12 indicates that the electric field is intensified at most by 2.4 times even for the porcelain spacer (ε_S = 7) by the external field E_0. Thus, the next chapter, the field mitigation is considered for the configuration of Figure 3.2, in which the field rises from the potential applied to the conductor.

CHAPTER IV

MITIGATION TECHNIQUE FOR THE FIELD AT THE CONTACT POINT

This chapter discusses three techniques for mitigating electric field at the contact point between the cable and spacer. The analysis is done only for the porcelain spacer, as the field condition is more severe than that in the case of HDPE spacer. The field strength at the contact point for HDPE spacer is used as the reference. I focus on the type SAC 50 mm^2 used for 22 kV systems and consider the thickness of the spacer equal to three times of the outer radius of the cable as a typical example.

4.1 Introduction

As previously mentioned in Chapter I, PEA uses the SAC overhead distribution lines mainly with porcelain and HDPE spacers at present. Each material has its own advantages and disadvantages. Porcelain spacers have good mechanical strength and usually do not deteriorate under thermal, chemical, electrical stresses. However, their problem is that the high field strength takes place at the contact point. A high electric field possibly causes partial discharge at the close vicinity of this point. Therefore, this chapter deals with the methods to reduce the contact-point electric field.

In connection to results obtained in Chapter III, the field is intensified by either decreasing the thickness of the spacer or increasing the dielectric constant of the spacer. Hence, to mitigate the field, I first consider the increase of the thickness and the decrease of the dielectric constant of the spacer. However, this solution is not practical, as it increases the weight of the spacer and the reduction of the dielectric constant of the spacer is difficult. I then try (1) increasing XLPE thickness of the conductor insulation, (2) adding an XLPE layer on the porcelain spacer and (3) covering the cable by a floating conductor. The first approach increases the distance between the conductor and the contact point. The second approach results in a smaller dielectric constant below the cable. The third approach uses a floating conductor, which does not deteriorate under partial discharge as much as dielectric materials. Note that only the electric field from the covered conductor under consideration is taken as the field source. The influence from other phase conductors is neglected.

4.2 Original Field Behavior

In this section, I focus on a particular case of the configuration in Figure 3.2, an insulated cylindrical conductor having total radius R and conductor radius R_C on a dielectric solid of thickness D_S. The case is for the type SAC 50 mm^2 used for 22 kV systems. In this case, R = 10.815 mm, R_C = 4.465 mm, R_C/R = 0.4129 (referred to Table 3.2), and $D_S = 3R$. The dielectric constant ε_S is either 2.2 or 7.0 for an HDPE or a porcelain spacer, respectively. The results have been discussed in Chapter 3; however, they will be presented here briefly for the purpose of reference.

The field strength is presented as a ratio to E_{c1}, the field strength at the contact point in the air side without supporting spacer. E_{c1} = 0.0455 kV/mm for the applied voltage V_0 = 1 kV at the conductor.

Figure 4.1 compares the electric distribution along the upper surface of the dielectric solid (see Figure 3.2) on the ε_A (air) side between the cases ε_S = 2.2 and ε_S = 7. The horizontal axis is the normalized distance (d_b/R) from the contact point. The field strength at the contact point is equal to $4.4E_{c1}$ and $2.1E_{c1}$ for ε_S = 7 and 2.2, respectively. That is, E_c is higher by 2.1 times when ε_S = 7 than that when ε_S = 2.2.

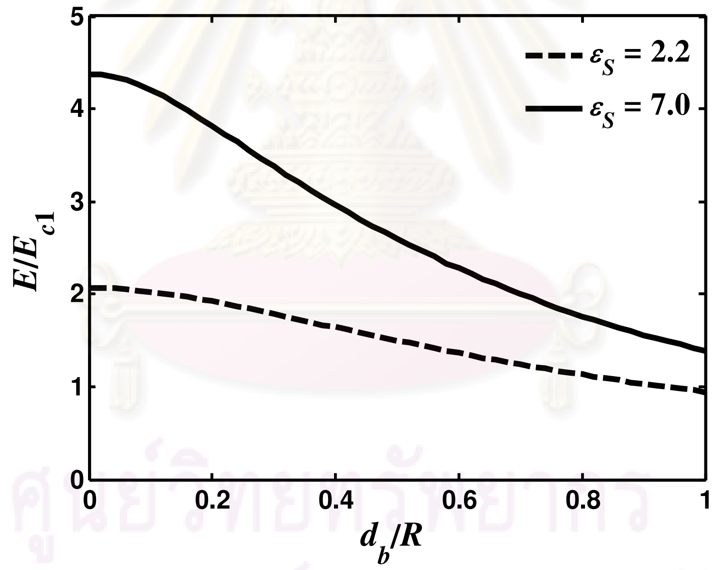

Figure 4.1: Normalized electric field along the upper surface of the dielectric solid.

4.3 Electric Field in Modified Configurations

In order to mitigate the field strength at the contact point for porcelain spacers, the replacing application of HDPE spacers is a solution. However, in this method, a few locations cannot be applied, for example, near the arms of tower requiring a strong mechanical strength and contaminative areas. In this section, I consider some fundamental measures to mitigate the electric field for the covered conductor on a porcelain spacer. A simple goal is to decrease the field strength E_c at the contact point to the value when the HDPE spacer is used. That is, E_c is to be reduced from $4.4E_{c1}$ to $2.1E_{c1}$, according to Figure 4.1. It should be noticed that we need to avoid the small air gap appeared from modification of the configuration, because the electric field enhances significantly there.

4.3.1 Increase in XLPE thickness

This section investigates the variation of the electric field with an additional thickness D_1 of the XLPE layer on porcelain spacer. This is equivalent to the increase in thickness of conductor insulation from configuration in Figure 3.2, as shown in Figure 4.2. The ratio D_1/R is a parameter influencing the electric field as I keep R_C/R = 0.4129 and $D_S = 3R$.

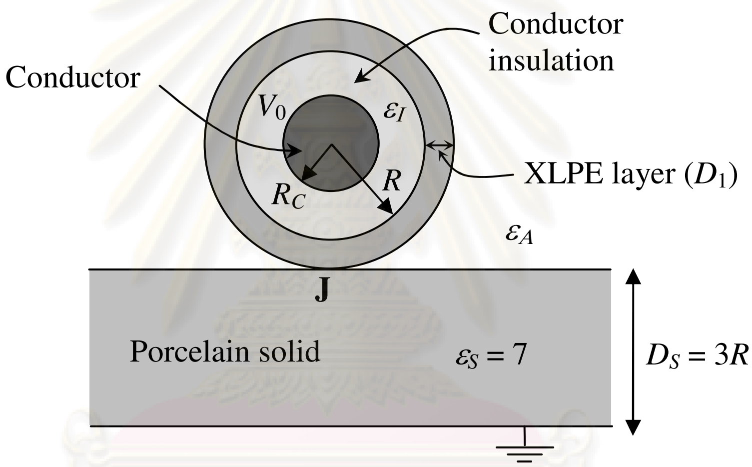

Figure 4.2: Addition of conductor insulation.

Figure 4.3 presents the electric-field ratio E/E_{c1} in the ε_A side at the contact point as a function of D_1/R. It is clear from the figure that E_c (solid line) decreases as the thickness D_1 increases. This is because of greater separation between the conductor and the spacer. Figure 4.3 demonstrates that with $D_1/R \approx 0.8$, we can reduce E_c to $2.1E_{c1}$. Note that a thin air gap may exist between the conductor insulation and the additional layer (at radius R) if the contact is imperfect between them. In this case, the electric field at the air gap is shown as the dotted line in Figure 4.3. We can see from the figure that the air-gap field still decreases with D_1 by a different relationship from that of E_c. For $D_1/R = 1$, the field at the air gap decrease to $2.1E_{c1}$.

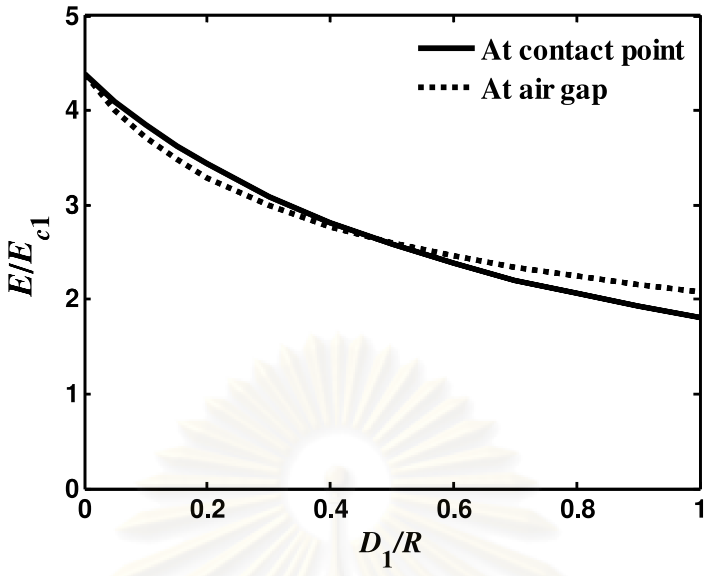

Figure 4.3: Electric-field ratio E/E_{c1} as a function of D_1/R.

4.3.2 Addition of an HDPE layer on porcelain spacer

Next, I consider the effects on the electric field by inserting an HDPE layer having thickness D_2 between the cable and porcelain spacer, as shown in Figure 4.4. Figure 4.5 shows the ratio of electric field to E_{c1} in relation with D_2/R. The figure demonstrates that the contact-point electric field E_c decreases with increasing D_2. Compare to Figure 4.3, we can see that the field reduction by D_2 is slower than that by increasing D_1. For example, in order to obtain $E_c = 2.1E_{c1}$, we need $D_2/R \approx 2.2$. The field characteristic in Figure 4.5 implies that increasing D_2/R from 3 does not efficiently reduce E_c. In the presence of an air gap between the inserted layer and the spacer, the electric field in the air gap is given as the dotted line in Figure 4.5. In this case, the air-gap field is always lower than the field at the contact point.

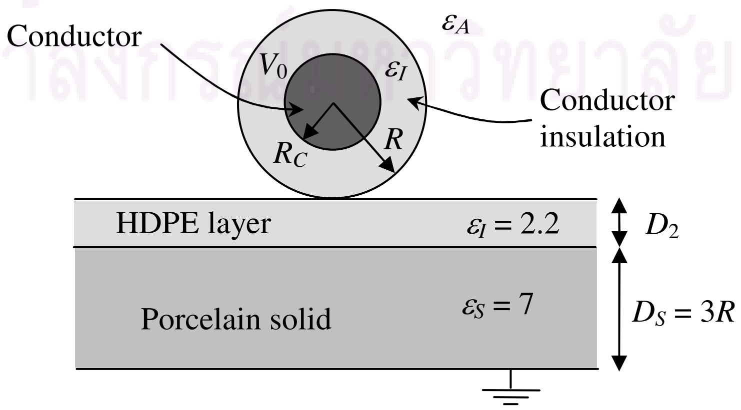

Figure 4.4: An HDPE layer inserted between the cable and porcelain spacer.

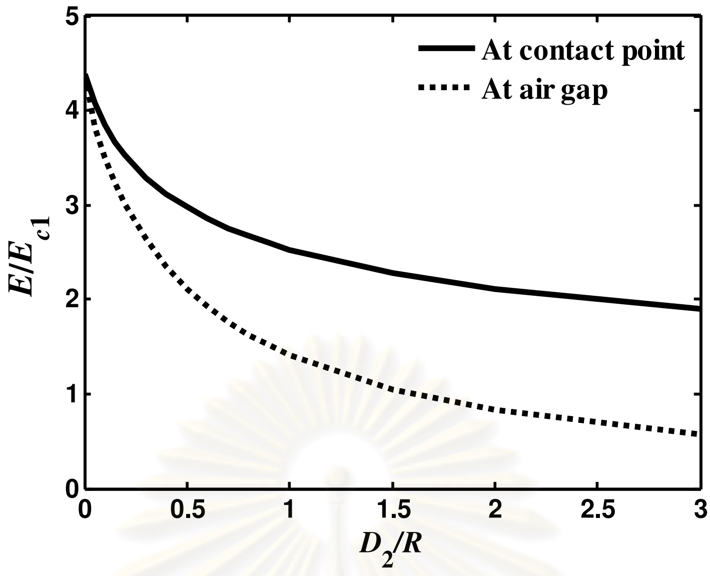

Figure 4.5: Electric-field ratio E/E_{c1} as a function of D_2/R.

4.3.3 Covering the cable with a floating conductor

Another measure expected to prevent the loss of conductor insulation due to the partial discharge is to cover the cable with a floating conductor. Figure 4.6 illustrates the configuration when the SAC is covered by a thin floating conductor layer.

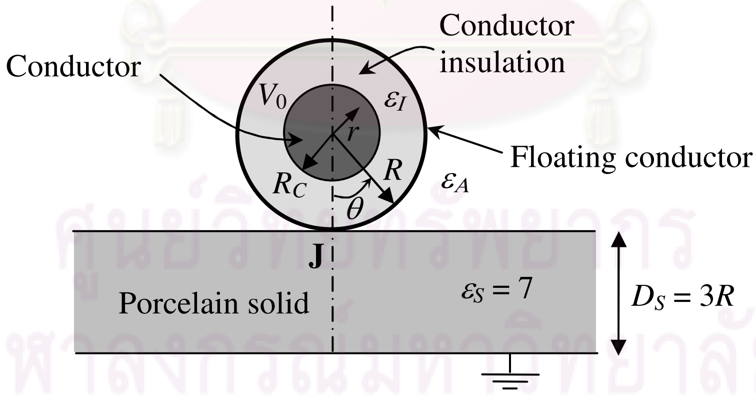

Figure 4.6: Cable covered by a thin floating conductor.

The floating conductor imposes the condition of equipotential on the outer surface of the conductor insulation (at $r = R$), which is in the calculation satisfied by applying (2.35) and (2.36) to the complex potentials. With the presence of the floating conductor, Figure 4.7 presents the change in potential distribution on the outer surface of the conductor insulation, where θ is the zenith angle measured from the contact point (see figure 4.6). It can be seen from Figure 4.7 that the floating conductor yields a potential value between the minimum and the maximum of the potential in the absence of the floating conductor (dotted line). As a result, the potential drop along vertical line from the inner conductor to the lower of the porcelain solid is smaller over the conductor insulation but larger over the porcelain solid by the application of the floating conductor.

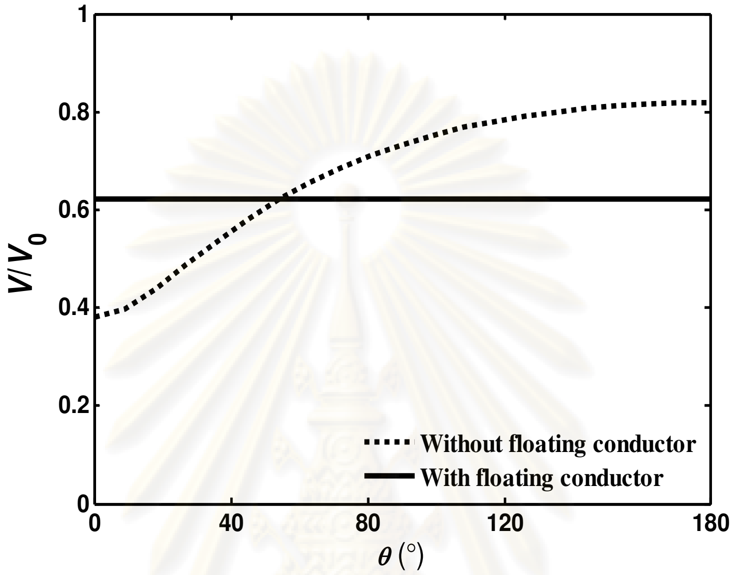

Figure 4.7: Distribution of the potential on the surface of the conductor insulation as a function of θ with and without the floating conductor.

Figure 4.8 presents the normal electric field at $r = R$ (see Figure 4.6) both on ε_A and on ε_I sides of the conductor insulation or the floating conductor if exist. The field values with and without the floating conductor are shown as the solid and the dotted lines, respectively. Compared to the electric field without the floating conductor, Figure 4.8 clearly shows that the electric field on the ε_A side is significantly higher near the contact point. On the other hand, the field on the ε_I side becomes lower by the presence of the floating conductor. Thus, the floating conductor mitigates the electric field on the ε_I side but intensifies the field on the ε_A side. This effect on the electric field may be roughly explained from the change in the potential drop in each region as illustrated in Figure 4.7. Thus, the application of the floating conductor may be an alternative for protecting the cable insulation, provided partial discharge in the air between the floating conductor and the spacer does not have adverse effect on the cable insulation. However, it should be noted that if an air gap exists in between the insulation and the floating conductor, then the air-gap field is equal to ε_I times of the field on the ε_I side shown in Figure 4.8. Note that the air-gap field is equal to $1.9E_{c1}$, whereas the field in the ε_I side without floating conductor is equal to 2 E_{c1}. In practice, the end of the floating conductor must be terminated properly to avoid excessively high field.

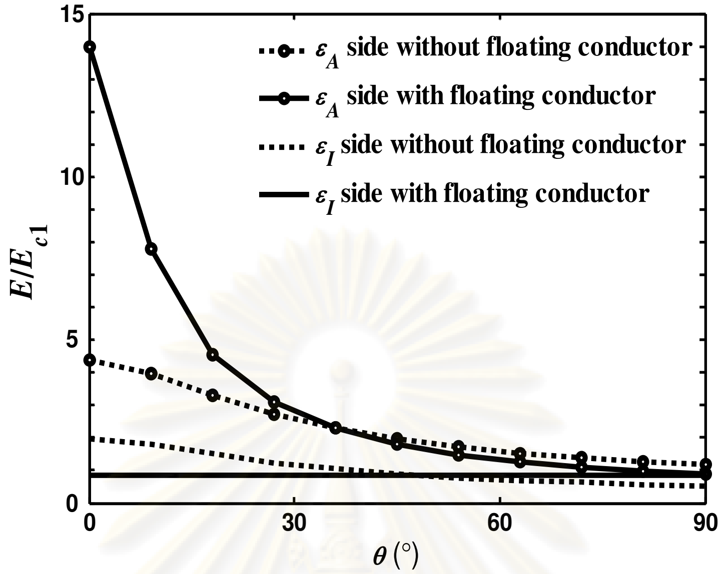

Figure 4.8: Electric field on the surface of the conductor insulation as a function of θ.

For the calculation presented here, I assumed a grounded potential at the lower surface of the dielectric solid for the calculation simplicity. Appendix D presents the application of filed mitigation techniques when an air gap between the spacer and the grounded plane is considered.

CHAPTER V

CONCLUSIONS

Up to now, a number of research works have analyzed the electric field at triple junctions by using either an analytical or a numerical method. However, the contact point with zero-contact angle between three dielectrics, such as that occurs where an insulated power conductor lies on a cable spacer, has not received much attention. Therefore, this thesis deals with the contact point problem.

The configuration is an insulated cylindrical conductor resting on a dielectric solid of finite thickness in a background medium (air). In this configuration, three dielectrics which include the conductor insulation, dielectric solid and background medium establish a triple junction at the contact point. The contact angle is zero due to a smooth contact. This configuration is a simple 2D model of SAC systems of overhead distribution lines at spacer position in practice. The insulated conductor and dielectric solid respectively represent the SAC and spacer. In order to realize high accuracy, the analytical method of multipole images is utilized for the field calculation. During the calculation process, the actual values of geometries and electrical parameters of SAC systems are applied to the configuration.

This thesis first studies the electric field behavior near the contact point, in which the focus is on the electric field at the contact point. The study treats two different sources: an applied potential at the core conductor and an external field caused by other phase conductors. In this study, the thickness D_S and dielectric constant ε_S of the dielectric solid are used as variables to investigate their effects on the electric field. The electric field behavior briefly summarized as follows:

- In the air side, the field strength is always maximal at the contact point and rapidly decreases with increasing distance from this point for all cases of ε_S.
- The maximum field at the contact point is intensified by either decreasing dimensional ratio of the thickness D_S of the dielectric solid to the outer radius R of the conductor insulation or increasing the dielectric constant ε_S of the dielectric solid.
- Under an external electric field by other phase conductors, the field strength at the contact point is typically much smaller than that under the applied potential.

Next, a practical case of the thickness D_S (D_S/R = 3) is chosen to examine approaches for reducing the intensification of electric field at the contact point. These approaches were carried out for the case of porcelain solid. For purpose of the examination, the electric field at the contact point by using HDPE solid is used as the reference. Three field mitigation techniques are given to discuss and concisely recapitulated as follows:

- The first one is to increase the XLPE insulation layer with an additional thickness D_1. The field in air side can be reduced to the reference field with D_1/R smaller than unity.
- The second one is to insert an HDPE layer between the cable and spacer with thickness D_2. The field reduction in air side by increasing D_2 is much slower than that by increasing D_1.
- The last one is to cover the cable by a thin floating conductor. The field is intensified about three times in the air side, but mitigated about two times in the side of the conductor insulation.

The results in this thesis can be applied to the insulation problems at position of the cable spacer in SAC systems of overhead distribution lines. The aim is to reduce the intensification of electric field at the contact point between the cable and spacer and to prevent the loss of the cable insulation.

The results here may be used as a base for extending work to the real, three-dimensional models, which is more complicated. The numerical methods may be used for the 3D field calculation.

REFERENCES

[1] Team IT Bangkokcable.com. 25&35 kV 90°C SAC ICEA S-66-524[Online]. (n.d.). Available from: http://www.bangkokcable.com/catalog/BCC_CATALOG/SACEN.HTML [2005].

[2] Report on the problems in the systems of space aerial cables after installation. *Internal communication*. The Provincial Electric Utility, Thailand, 2009.

[3] T. Takuma, and T. Kawamoto. Field behavior at a triple junction in composite dielectric arrangements. *IEEE Trans. Electrical Insulation* 26 (1991) 500-509.

[4] B. Techaumnat, S. Hamada and T. Takuma. Electric field behavior near a contact point in the presence of volume conductivity. *IEEE Trans. Electrical Insulation* 8 (2001) 930-935.

[5] B. Techaumnat and T. Takuma. Field intensification at the contact point between a conducting plane and a spheroid or an elliptic cylinder. *Proceedings of 2005 International Symposium on Electrical Insulating Materials*, B5-4 (2005) 808-811.

[6] T. Takuma and T. Kawamoto. Field enhancement at a triple junction in arrangements consisting of three media. *IEEE Trans. Electrical Insulation* 14 (2007) 566-571.

[7] B. Techaumnat and T. Takuma. Calculation of the electric field for lined-up spherical dielectric particles. *IEEE Trans. Electrical Insulation* 10 (2003) 623-633.

[8] B. Techaumnat, S. Hamada and T. Takuma. Electric field behavior near a zero-angle contact point in the presence of surface conductivity. *IEEE Trans. Electrical Insulation* 9 (2002) 537-543.

[9] T. Takuma and T. Kawamoto. Field intensification near various points of contact with a zero contact angle between a solid dielectric and an electrode. *IEEE Trans. Power Apparatus System*, vol. PAS-103, no. 9 (1984) 2486-2494.

[10] T. Takuma and B. Techaumnat. Electric field in composite dielectrics, Springer, 2010.

[11] T. Takuma, T. Kouno and H. Matsuda. Field behavior near singular points in composite dielectric arrangements. *IEEE Trans. Electrical Insulation* EI-13 (1978) 426-435.

[12] T. Kawamoto, T. Takuma, H. Goshima, H. Shinkai and H. Fujinami. Triple-junction effect and its electric field relaxation in three dielectrics. *Electrical Engineering in Japan*, 167 (2009).

[13] E. Kreyszing. Advanced Engineering Mathematics, ninth ed., Wiley, Singapore, 2006.

[14] V. Rokhlin. Rapid solution of integral equations of classical potential theory. *Journal Computational Physics* 60 (1983) 187-2007.

[15] L. Greengard and V. Rokhlin. A fast algorithm for particle simulations. *Journal Computational Physics* 73 (1987) 325-348.

[16] B. Techaumnat, and T. Takuma. Calculation of electric field in two-dimensional arrangements by the method of multipole images. *Journal of Electrostatics* 64 (2006) 706-716.

[17] Neal A. Smith. Design considerations of spacers for aerial spacer cable. *IEEE Trans. Electrical Insulation* EI-4 (1969), 12-17.

[18] B. Techaumnat, and T. Takuma. Electric field behavior near a point of contact for a spherical conductor lying on a thin dielectric plate. *15th Asian Conference on Electrical Discharge*, pp.140-143.China, 2010.

APPENDICES

APPENDIX A

Field Strength and Field Ratio at the Contact Point for Various Types of SAC

Table A.1: Field strength E_c (kV/mm) when $V_0 = 22\sqrt{2}/\sqrt{3}$ and field ratio E_c/E_{c1} at the contact point for SAC50-22kV.

a. E_c

ε_S	D_S/R																
	0	0.001	0.003	0.01	0.04	0.1	0.5	1	2	4	10	20	50	100	200	1000	10000
1.0	6.34	6.30	6.22	5.96	5.14	4.16	2.10	1.44	0.99	0.72	0.51	0.42	0.34	0.29	0.26	0.21	0.16
1.5	6.34	6.31	6.26	6.07	5.46	4.65	2.69	1.96	1.43	1.08	0.79	0.66	0.53	0.47	0.42	0.34	0.26
2.2	6.34	6.32	6.28	6.16	5.70	5.05	3.28	2.54	1.95	1.53	1.17	0.98	0.81	0.72	0.65	0.52	0.41
7.0	6.34	6.34	6.32	6.28	6.11	5.84	4.89	4.37	3.85	3.39	2.90	2.60	2.29	2.09	1.93	1.64	1.34

b. E_c/E_{c1}

ε_S	D_S/R																
	0	0.001	0.003	0.01	0.04	0.1	0.5	1	2	4	10	20	50	100	200	1000	10000
1.5	1.00	1.00	1.01	1.02	1.06	1.12	1.28	1.37	1.44	1.50	1.55	1.58	1.60	1.60	1.61	1.62	1.62
2.2	1.00	1.00	1.01	1.03	1.11	1.22	1.57	1.77	1.96	2.13	2.29	2.36	2.42	2.45	2.48	2.51	2.54
7.0	1.00	1.01	1.02	1.05	1.19	1.41	2.34	3.04	3.87	4.72	5.68	6.25	6.82	7.14	7.41	7.88	8.33

Table A.2: Field strength E_c (kV/mm) when $V_0 = 22\sqrt{2}/\sqrt{3}$ and field ratio E_c/E_{c1} at the contact point for SAC185-22kV.

a. E_c

ε_S	D_S/R																
	0	0.001	0.003	0.01	0.04	0.1	0.5	1	2	4	10	20	50	100	200	1000	10000
1.0	6.48	6.43	6.33	6.02	5.06	3.94	1.80	1.19	0.80	0.57	0.39	0.32	0.26	0.22	0.20	0.16	0.12
1.5	6.48	6.45	6.38	6.16	5.43	4.49	2.38	1.67	1.18	0.87	0.63	0.51	0.42	0.36	0.32	0.26	0.20
2.2	6.48	6.46	6.41	6.26	5.71	4.95	2.99	2.23	1.66	1.27	0.95	0.79	0.65	0.57	0.51	0.41	0.32
7.0	6.48	6.48	6.46	6.41	6.21	5.88	4.75	4.14	3.57	3.08	2.57	2.28	1.98	1.79	1.64	1.38	1.12

b. E_c/E_{c1}

ε_S	D_S/R																
	0	0.001	0.003	0.01	0.04	0.1	0.5	1	2	4	10	20	50	100	200	1000	10000
1.5	1.00	1.00	1.01	1.02	1.07	1.14	1.32	1.40	1.48	1.54	1.59	1.61	1.63	1.64	1.64	1.65	1.66
2.2	1.00	1.00	1.01	1.04	1.13	1.26	1.66	1.87	2.08	2.25	2.40	2.47	2.53	2.56	2.58	2.61	2.64
7.0	1.00	1.01	1.02	1.06	1.23	1.49	2.64	3.48	4.46	5.44	6.52	7.14	7.74	8.08	8.35	8.81	9.24

Table A.3: Field strength E_c (kV/mm) when $V_0 = 33\sqrt{2}/\sqrt{3}$ and field ratio E_c/E_{c1} at the contact point for SAC50-33kV.

a. E_c

ε_S	D_S/R																
	0	0.001	0.003	0.01	0.04	0.1	0.5	1	2	4	10	20	50	100	200	1000	10000
1.0	7.83	7.79	7.69	7.37	6.40	5.21	2.69	1.86	1.30	0.94	0.67	0.55	0.45	0.39	0.35	0.28	0.22
1.5	7.83	7.80	7.74	7.52	6.78	5.81	3.43	2.52	1.86	1.41	1.04	0.86	0.71	0.62	0.56	0.45	0.35
2.2	7.83	7.81	7.77	7.61	7.07	6.29	4.16	3.25	2.52	1.99	1.52	1.29	1.07	0.95	0.85	0.69	0.54
7.0	7.83	7.83	7.82	7.76	7.56	7.24	6.11	5.48	4.86	4.31	3.70	3.33	2.94	2.70	2.50	2.12	1.75

b. E_c/E_{c1}

ε_S	D_S/R																
	0	0.001	0.003	0.01	0.04	0.1	0.5	1	2	4	10	20	50	100	200	1000	10000
1.5	1.00	1.00	1.01	1.02	1.06	1.11	1.27	1.36	1.43	1.49	1.54	1.57	1.59	1.60	1.60	1.61	1.62
2.2	1.00	1.00	1.01	1.03	1.10	1.21	1.55	1.74	1.94	2.10	2.26	2.33	2.40	2.43	2.45	2.49	2.51
7.0	1.00	1.01	1.02	1.05	1.18	1.39	2.27	2.94	3.74	4.56	5.49	6.04	6.60	6.93	7.19	7.66	8.12

Table A.4: Field strength E_c (kV/mm) when $V_0 = 33\sqrt{2}/\sqrt{3}$ and field ratio E_c/E_{c1} at the contact point for SAC185-33kV.

a. E_c

ε_S	D_S/R																
	0	0.001	0.003	0.01	0.04	0.1	0.5	1	2	4	10	20	50	100	200	1000	10000
1.0	8.07	8.01	7.89	7.53	6.38	5.03	2.38	1.59	1.08	0.77	0.54	0.44	0.35	0.30	0.27	0.21	0.17
1.5	8.07	8.03	7.95	7.69	6.83	5.71	3.11	2.21	1.58	1.17	0.85	0.70	0.57	0.50	0.44	0.35	0.27
2.2	8.07	8.04	7.99	7.81	7.16	6.26	3.87	2.92	2.20	1.70	1.27	1.06	0.87	0.77	0.69	0.55	0.43
7.0	8.07	8.06	8.05	7.99	7.75	7.36	6.02	5.29	4.60	3.99	3.36	2.98	2.60	2.37	2.17	1.82	1.48

b. E_c/E_{c1}

ε_S	D_S/R																
	0	0.001	0.003	0.01	0.04	0.1	0.5	1	2	4	10	20	50	100	200	1000	10000
1.5	1.00	1.00	1.01	1.02	1.07	1.13	1.31	1.39	1.47	1.53	1.58	1.60	1.62	1.63	1.63	1.64	1.65
2.2	1.00	1.00	1.01	1.04	1.12	1.24	1.63	1.84	2.04	2.21	2.36	2.44	2.50	2.53	2.55	2.58	2.60
7.0	1.00	1.01	1.02	1.06	1.21	1.46	2.53	3.33	4.26	5.20	6.24	6.84	7.43	7.77	8.04	8.50	8.94

APPENDIX B

Capacitance Model for Field Estimation

Capacitance models are sometimes applied to the estimation of the electric field near a triple junction [9, 18]. From the estimation, we can obtain a rough value of the discharge inception voltage. This appendix presents the estimation of the electric field near the contact point J in Figure 3.2 by using the capacitance model. As an example, the estimation is done for the case of a 22 kV 50 mm^2 SAC on a dielectric solid having D_S = 3R. The parameters used for the estimation are shown in Figure B.1. In the figure, four points a, b, c and d lie on the dashed line. The points a and b are at radius R_C and R, respectively. The points c and d are at the upper surface and lower surface of the dielectric solid, respectively. In addition, the variable r is a distance between J and c.

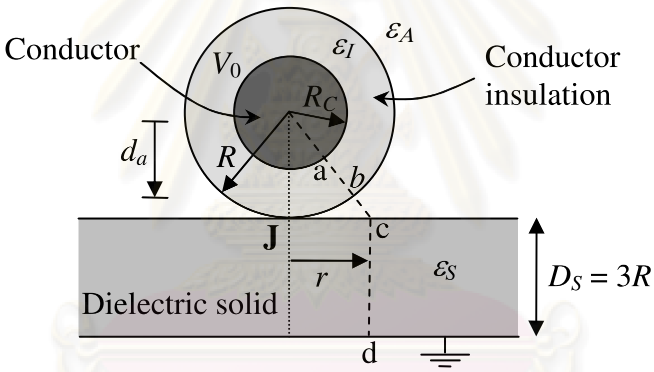

Figure B.1: Configuration for field estimation.

In the capacitance model, the field strength is evaluated by dividing the applied voltage between the conductor insulation, the air medium and the dielectric solid as capacitive impedances in series. The approximation assumes that the field distribution is almost uniform inside each dielectric medium along the dashed line. It gives the field strength E in the air medium as follows:

$$E = \frac{V_0}{\overline{bc} + \overline{ab}\left(\varepsilon_A/\varepsilon_I\right) + \overline{cd}\left(\varepsilon_A/\varepsilon_S\right)}, \tag{B.1}$$

where $\overline{ab} = R - R_C$, $\overline{bc} = \sqrt{R^2 + r^2} - R$ and $\overline{cd} = D_S$. The points a, b, c and d are indicated in Figure B.1. Thus, the field strength E_c at the contact point according to $\overline{bc} = 0$ is expressed as

$$E_c = \frac{V_0}{(R - R_C)(\varepsilon_A/\varepsilon_I) + D_S(\varepsilon_A/\varepsilon_S)} . \tag{B.2}$$

Besides, near the point J, i.e., when $\overline{bc}$ is small, the distance $\overline{bc}$ can be approximated equal to $r^2/2R$. The expression in (B.1) becomes

$$E = \frac{V_0}{r^2/2R + (R - R_C)(\varepsilon_A/\varepsilon_I) + D_S(\varepsilon_A/\varepsilon_S)} \tag{B.3}$$

The estimation of electric field is done for two cases of ε_S = 2.2 and 7. The field distribution near J in the air side approximated by (B.3) is compared with that calculated by multipole image method in Figure B.2. The field is normalized by V_0/R, and the distance r is normalized by R. It can be seen from Figure B.2 that the estimate field (solid line) is always lower than that obtained by the image method (dotted line). The difference of the estimate field from the accurate one is maximal at the contact point and higher for lower ε_S. The difference is as high as 40% and 33% when ε_S = 2.2 and 7, respectively.

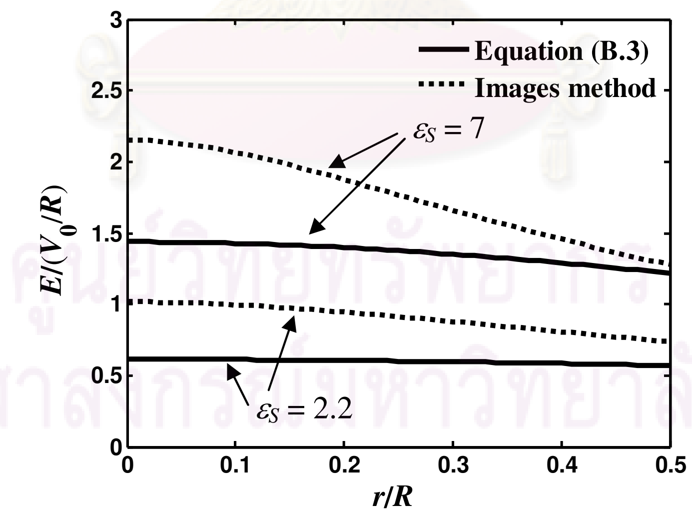

Figure B.2: Comparison between the approximated and the accurate electric field.

Figures B.3 and B.4 present the potential drop and field distribution in the conductor insulation and dielectric solid along vertical line at J by the image method, respectively. From the accurate values of the potential in Figure B.3, I determine the error of the potential drop in conductor insulation (ξ_I) and in the dielectric solid (ξ_S). For $\varepsilon_S = 2.2$, $\xi_I = 53\%$ and $\xi_S = 27\%$; whereas $\xi_I = 39\%$ and $\xi_S = 63\%$ for $\varepsilon_S = 7$.

Note that by using the capacitance model, the approximate potential drop in the conductor insulation and in the dielectric solid is equal to $0.16V_0$ and $0.84V_0$ for $\varepsilon_S = 2.2$, and $0.38V_0$ and $0.62V_0$ for $\varepsilon_S = 7$.

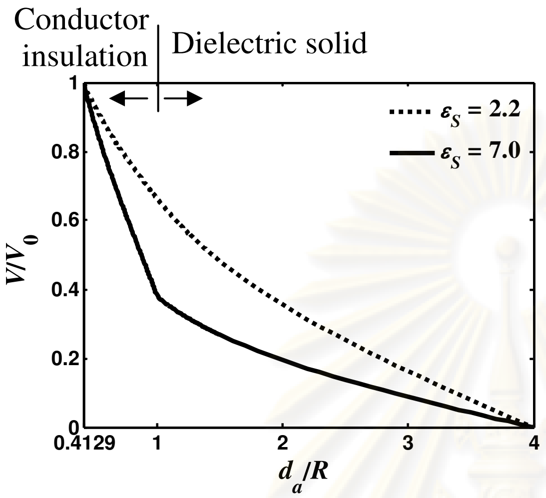

Figure B.3: Potential drop in the conductor insulation and the dielectric solid.

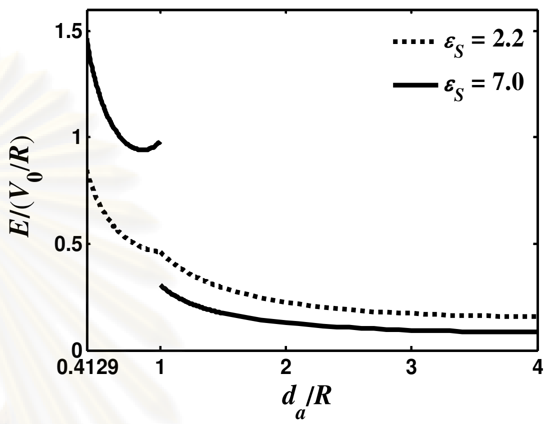

Figure B.4: Field distribution inside the conductor insulation and the dielectric solid.

In Figure B.4, I calculate the difference of the maximum and minimum values of electric field (in comparison with their average value) inside the conductor insulation (ω_I) and in the dielectric solid (ω_S). For $\varepsilon_S = 2.2$, $\omega_I = 59\%$ and $\omega_S = 98\%$; whereas $\omega_I = 44\%$ and $\omega_S = 113\%$ for $\varepsilon_S = 7$.

From the accurate values of the potential and electric field, we can see that the error occurred in the estimation of the field at J is because of the nonunifrom field in two dielectric media of the conductor insulation and dielectric solid. The nonunifrom degree of the electric field is expressed by the coefficients ω and ξ. The error is governed by the nonunifrom field in the conductor insulation. This proof can be found in case of $\varepsilon_S = 2.2$ as both $\omega_I = 59\%$ and $\xi_I = 53\%$ are higher than $\omega_I = 39\%$ and $\xi_I = 44\%$ for $\varepsilon_S = 7$, respectively.

From the results obtained here, I demonstrate that in a practical case of $D_S = 3R$ the electric field at contact point in Figure 3.2 can not be approximated accurately by the capacitance model.

APPENDIX C

External Field due to Other Phase Conductors

In overhead-line distribution systems using SAC, the cable spacers are suspended by grounded messenger wires, as shown in Figure C.1. In Figure C.1, the messenger wire is at the top end, and the three-phase cables are held at the other ends. There are two common shapes of the spacer, i.e., cross-shape for porcelain spacers and lozenge for polyethylene spacers. The dimension of spacer varies between manufactures. The height of the spacer above the ground level depends on the system voltages and geographical conditions. However, both the dimensions of spacer and its height are much larger than the dimension of the phase conductor. Therefore, the variation of their values does not significantly change the external field to which each phase conductor is subjected. As an example, I consider the real dimensions of a polyethylene spacer for the calculation of external field.

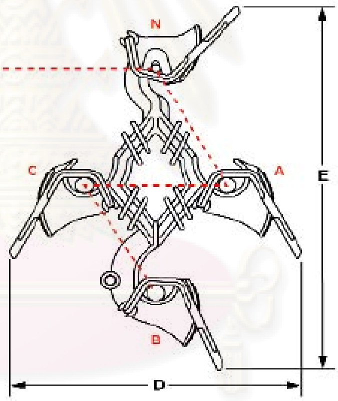

AN	304 mm.
AC	292 mm.
BC	292 mm.

Figure C.1: Polyethylene spacer [2].

Figure C.2 shows a cross section of 22 kV 3 phase overhead distribution lines with the height above ground of the lowest phase equal to 8 m. For the purpose of estimation, the influence of the spacer is neglected, although the XLPE insulation layer of the SAC is still considered. The electric field varies linearly with the potential, and the potential on the overhead line is three-phase alternating voltages. When the potential at one phase is maximal, the remaining phases are at a half of that maximum value. Therefore, I take potential values at the phases equal to $V_{\text{system}}/\sqrt{6}$, where V_{system} = 22 or 33 kV to estimate the external field.

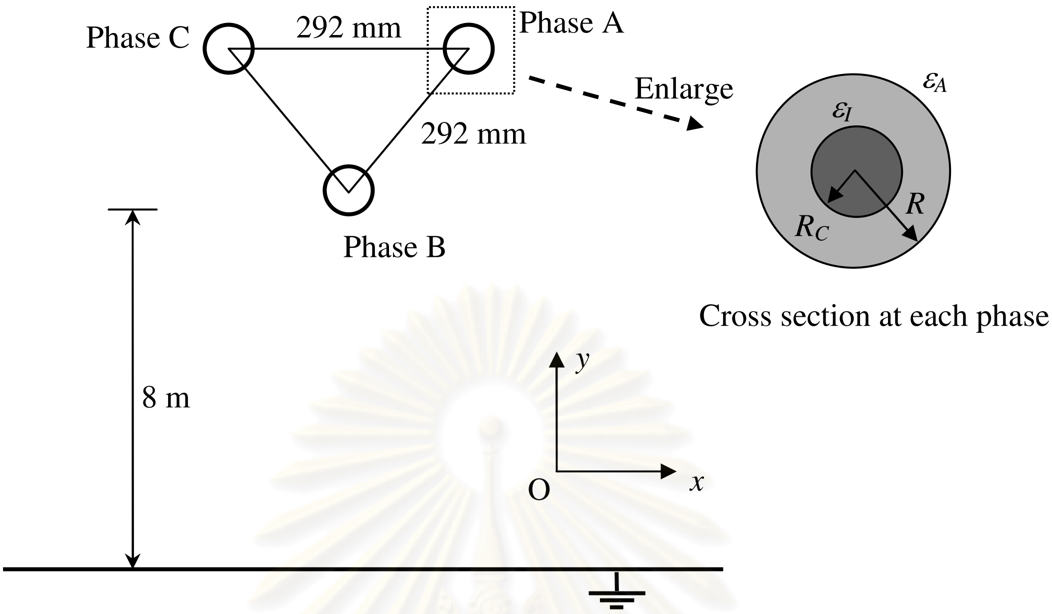

Figure C.2: Cross section of 22-kV 3-phase overhead distribution lines.

Using the parameters of SAC 50 mm^2 used for 22 kV as specified in Section 3.1, the estimated external field is calculated. The results are shown in Table C.1 in which the electric field is expressed in the form of $E_{x0} + iE_{y0}$. The directions of x and y are referred to Figure C.2.

Table C.1: Electric field (V/mm) in the form of $E_{x0} + iE_{y0}$ estimated from other phase potentials.

Position of source	**Position of calculation**		
	Phase A	Phase B	Phase C
Phase B	$2 + 3.4i$	#	$-2 + 3.4i$
Phase C	$4 - 0.1i$	$2 - 3.5i$	#

From the Table C.1, it demonstrates that magnitude of electric field approximates few V/mm, whereas the maximum electric field at triple junction resulted from the phase potential in the section 3.2 is around few kV/mm (see Figure 3.8), in particular, approximately 1000 times.

APPENDIX D

Results in the Presence of Air Gap Between the Dielectric Solid and the Grounded Plane

D.1 Electric field at the contact point

This appendix discusses the techniques of field mitigation when the grounded plane is separated from the dielectric solid as shown in Figure D.1. The ratio $D_g/R = 740$ is used for the calculation. This ratio is referred from the height of the lowest phase conductor as mentioned in Appendix C.

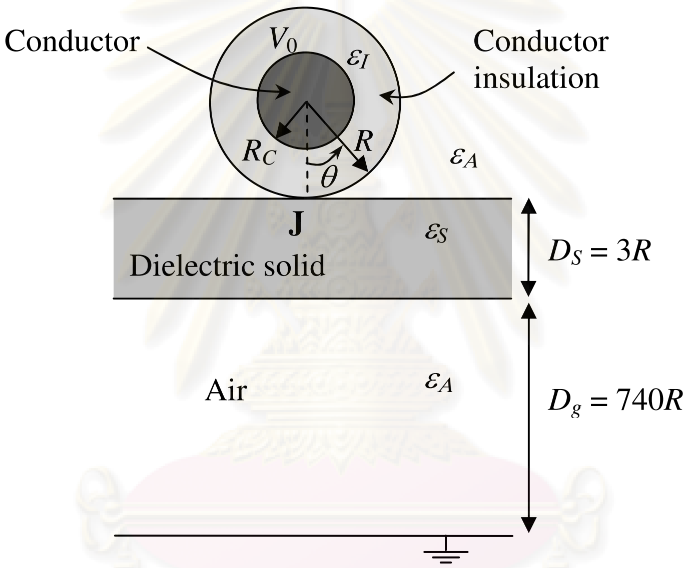

Figure D.1: Configuration used for analysis.

For studying field mitigation, I first determine the electric field E_c at the contact point in the air side in the configuration of Figure D.1 for both cases of $\varepsilon_S = 2.2$ and 7. The field is normalized by E_{c1} defined as the field at the contact point in the ε_A side for $\varepsilon_S = 1$. ($E_{c1} = 0.012$ kV/mm for $V_0 = 1$ kV.) The results of the calculation shown that $E_c = 3E_{c1}$ as $\varepsilon_S = 7$ and $E_c = 1.7E_{c1}$ as $\varepsilon_S = 2.2$. That is, E_c is higher by 1.8 times when $\varepsilon_S = 7$ than that when $\varepsilon_S = 2.2$.

D.2 Electric field in the modified configurations

Similar to Chapter 4, three modified configurations are analyzed for purpose of field mitigation.

i. Increase in XLPE thickness

Figure D.2 presents the variation of the electric field by increasing in D_1 (see Figure 4.2). The figure demonstrates that E_c (solid line) can be reduced to $1.7E_{c1}$ with $D_1/R \approx 0.65$. Compare to case without the separation between the dielectric solid and the plane in the section 4.3.1, D_1/R is lower. For the electric field in the air gap at radius of R (dotted line), the field at the air gap decreases approximately to $1.7E_{c1}$ with $D_1/R = 1$.

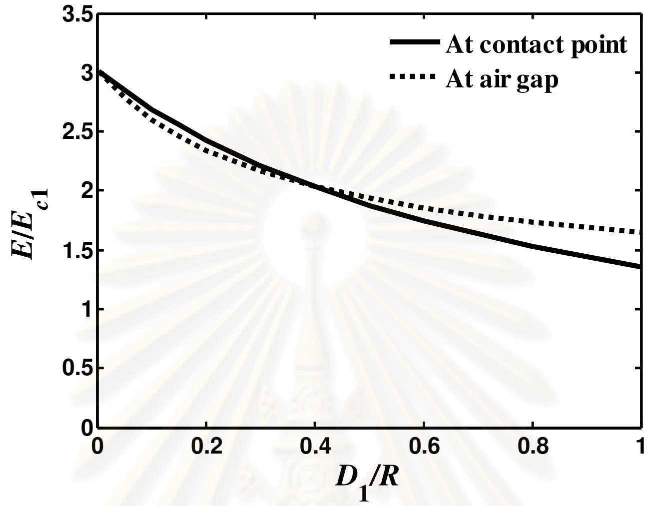

Figure D.2: Electric field ratio E/E_{c1} as a function of D_1/R.

ii. Addition of an HDPE layer on porcelain solid

Figure D.3 presents the effect of electric field in relation with D_2/R (see Figure 4.4). Figure D.3 indicates that E_c can not be reduced to $1.7E_{c1}$ even with $D_2/R = 3$. In this case, the characteristic of air-gap field distribution is similar to that in the section 4.3.2.

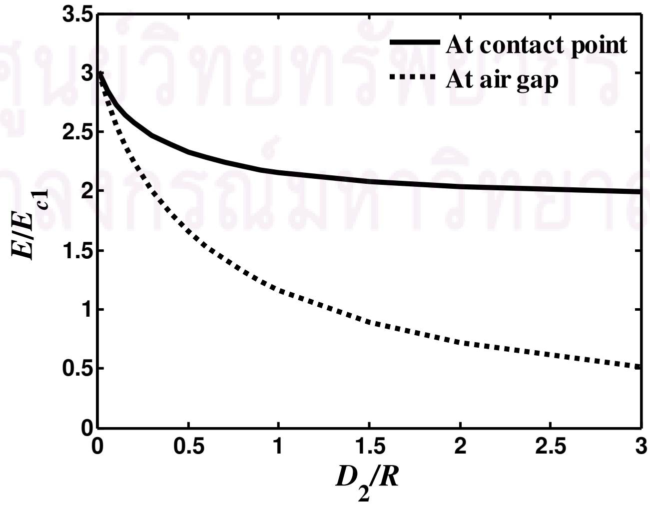

Figure D.3: Electric field ratio E/E_{c1} as a function of D_2/R.

iii. Covering the cable with a floating conductor

Figures D.4 shows normal electric field on surface of the conductor insulation at $r = R$ (see Figure 4.6) in solid line. It is can seen from the figure that the characteristic of the electric field is similar to that in the case that the air gap D_g is neglected in Figure 4.8.

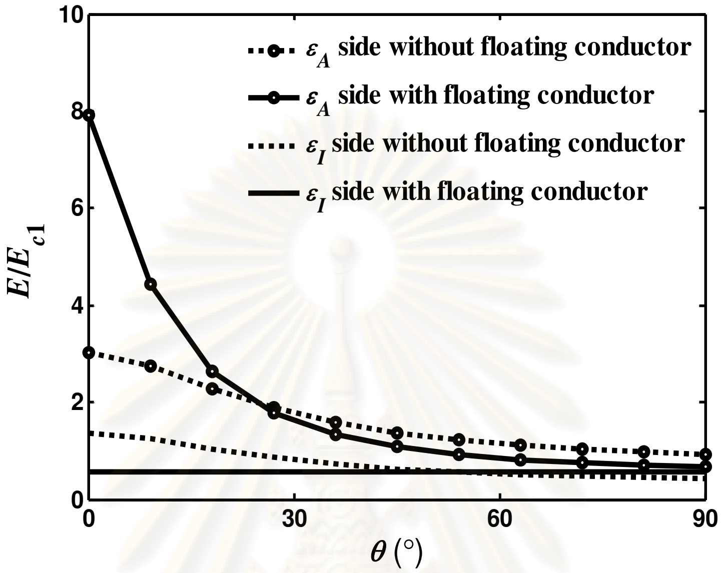

Figure D.4: Electric field on the surface of the conductor insulation as a function of θ.

BIOGRAPHY

Viet Quoc Huynh was born in Ben Tre, Vietnam, in 1985. He received his Bachelor's degree in electrical engineering from Ho Chi Minh City University of Technology, Vietnam, in 2008. He has been granted a scholarship by the AUN/SEED-Net (www.seed-net.org) to pursue his Master's degree in electrical engineering at Chulalongkorn University, Thailand, since 2009. He conducted his graduate study with the High Voltage Laboratory, Department of Electrical Engineering, Faculty of Engineering, Chulalongkorn University. His research interest focuses on investigation of triple junction problems with a zero-contact angle in high-voltage insulation systems by the multipole image method.